INTERNATIONAL JOURNAL FOR NUMERICAL METHODS IN FLUIDS
Int. J. Numer. Meth. Fluids 2009; **61**:57–105
Published online 5 November 2008 in Wiley InterScience (www.interscience.wiley.com). DOI: 10.1002/fld.1944

A compact high-order HLL solver for nonlinear hyperbolic systems

G. Capdeville*, †

Département de Mécanique des fluides, Ecole Centrale de Nantes, France

SUMMARY

We present a new finite-volume method for calculating complex flows on non-uniform meshes. This method is designed to be highly compact and to accurately capture all discontinuities that may arise within the solution of a nonlinear hyperbolic system.

In the first step, we devise a fourth-degree Hermite polynomial to interpolate the solution. The coefficients defining this polynomial are calculated by using a least-square method. To introduce monotonicity conditions within the procedure, two constraints are added into the least-square system. Those constraints are derived by locally matching the high-order Hermite polynomial with a low-order TVD polynomial. To emulate these constraints only in regions of discontinuities, data-depending weights are defined; these weights are based upon normalized indicators of smoothness of the solution and are parameterized by an $O(1)$ quantity. The reconstruction so generated is highly compact and is fifth-order accurate when the solution is smooth; this reconstruction becomes first order in regions of discontinuities.

In the second step, this reconstruction is inserted in an HLL approximate Riemann solver. This solver is designed to correctly capture all discontinuities that may arise into the solution. To this aim, we introduce the contribution of a possible contact discontinuity into the HLL Riemann solver.

Thus, a spatially fifth-order non-oscillatory method is generated. This method evolves in time the solution and its first derivative. In a one-dimensional context, a linear spectral analysis and extensive numerical experiments make it possible to assess the robustness and the advantages of the method in computing multi-scale problems with embedded discontinuities. Copyright © 2008 John Wiley & Sons, Ltd.

Received 27 March 2008; Revised 4 September 2008; Accepted 5 September 2008

KEY WORDS: least-square reconstruction; hermite polynomial; data-depending weight; hyperbolic systems; non-uniform meshes; upwind discretization; aeroacoustics; HLL Riemann solver; contact discontinuity; shock wave

*Correspondence to: G. Capdeville, Département de Mécanique des fluides, Ecole Centrale de Nantes, 1, rue de la Noë, B.P. 92101, 44321 Nantes cedex 3, France.
†E-mail: guy.capdeville@ec-nantes.fr

1. INTRODUCTION

Nowadays, there is a growing need for high-order numerical methods in computational fluid dynamics. Aeroacoustics, turbulence modelling or magneto-hydrodynamics are domains for which high-order accuracy is strongly needed. Flow problems with intricate structures and a broad range of characteristic scales cannot be efficiently modelled by conventional second-order numerical methods; even on very fine meshes, these methods are unable to correctly extract a weak signal from the mean flow.

Relying on a finite-volume framework, the definition of a reconstruction procedure of the solution from its cell-averaged values is the first important task in obtaining a high-order numerical method.

Ideally, the reconstruction should ensure high-order accuracy, even on non-Cartesian meshes, while preserving the monotonicity of the solution.

Starting from the pioneering work of Van-Leer in 1977 [1], much work has been done on this topic. In 1987, Harten *et al.* developed the henceforth classic category of essentially non-oscillatory (ENO) schemes [2]. Later, Liu *et al.* [3], improved ENO schemes by developing the class of weighted essentially non-oscillatory (WENO) schemes (see [4] for a good overview on these topics).

However, in spite of their vast field of application, standard WENO schemes still have deficiencies: due to the width of their numerical stencil, the extension to non-Cartesian meshes is somewhat cumbersome; moreover, a wide stencil is not optimum neither in terms of an accurate treatment of weak fluctuations, nor concerning the imposition of boundary conditions.

Considering these insufficiencies, we propose a new approach that is designed to be compatible with multi-dimensional extensions on non-Cartesian meshes. To preserve the compactness of the stencil, this approach relies upon Hermite polynomials; these polynomials are constructed by a least-square methodology.

The use of a least-square reconstruction to build a high-order finite-volume scheme is not a novelty. A few years ago, Barth [5, 6], produced a great amount of article on this subject. He constructed an upwind finite-volume scheme, via a Godunov's method, to be utilized on unstructured meshes.

In [5], Barth gave general indications to construct a least-square method including data-dependent weights. However, he did not develop such a possibility into his work. This is the merit of Ollivier-Gooch to have concretized this idea [7].

Ollivier-Gooch devised a least-square reconstruction scheme suited for unstructured meshes. Then, he modified this reconstruction to satisfy the ENO property. This modification was ensured by a data-dependent weighting that used the residual of the least-square problem—in order to detect stencils with non-smooth data—and the local gradient of the solution—in order to determine which data within that stencil should be excluded (see [7] for details).

In this manner, the resulting scheme ('DD-L2-ENO' scheme) was demonstrated to be uniformly accurate, even in the presence of discontinuities, and allowed only asymptotically small overshoots.

However, as Ollivier-Gooch noticed in his article, such a scheme is not designed to produce high-order accurate solutions: required stencils' sizes for such high-accuracy grow very rapidly; in other words, the numerical stencil is not compact enough. Moreover, this procedure necessitates to solve two least-square problems. Indeed, a least-square problem is first necessary for evaluating the residual and then for calculating data-dependent weights; a second least-square problem, modified by those weights, is then solved to give the derivatives needed by the reconstruction. This feature results in a very costly method, especially when the procedure is used for systems.

DOI: 10.1002/fld

Considering the work of Barth and Ollivier-Gooch, our point of view is different: instead of constructing a polynomial and then to modify it in order to preserve the monotonicity, we introduce a monotonicity principle *within* the calculation of the polynomial coefficients. This is achieved by using a least-square method with specific additional constraints.

Keeping in mind the necessary compactness of the discretization, the method we developed has the following features:

- A Hermite polynomial reconstruction using the solution and its first derivative is devised. In a finite-volume context, this reconstruction is first defined to preserve the average. The numerical stencil is selected so that the interpolated solution using this reconstruction, is fifth-order accurate—in terms of truncature error—in regions of smoothness.
- Instead of using Hermite basis functions as in [8], we utilize a least-square methodology to calculate the polynomial coefficients. When solved without any modification, the resulting system generates a fifth-order approximation in regions of smoothness and Gibbs-like phenomena in regions of discontinuities.
- To introduce a monotonicity condition into this reconstruction, we add two constraints to the initial system. These constraints are generated by imposing that the oscillatory reconstruction locally coincides with a monotone reconstruction. This monotone reconstruction is obtained from a TVD condition.
- To emulate these constraints only in regions of discontinuities, we define a normalized smoothness indicator that is used to compute data-depending weights. Then, those quantities are used to weight the constraints of monotonicity.

In this manner, we are able to construct a Hermite least-square monotone (HLSM) reconstruction that has the following properties:

- Compactness of the numerical stencil: on a three-points stencil, we can devise a fifth-order accurate reconstruction by using the solution and its first derivative.
- Owing to the least-square procedure, it is possible to deal with irregular meshes without sacrificing accuracy.
- A monotone reconstruction: locally the reconstruction degrades to a TVD approximation, as soon as a discontinuity appears into the solution. This means that the resulting scheme evolves between a fifth-order accuracy and a first-order accuracy at the location of a discontinuity.
- A smooth evolution between high accuracy and low accuracy: this faculty is ensured by the definition of the weights and is enforced by the smoothing properties inherent to a least-square method.
- Computation of only one least-square problem to produce a monotone reconstruction.
- The numerical stencil is never modified. Only the polynomial coefficients are altered to introduce monotonicity principles.

In the second step, this interpolation method is inserted into an HLL Riemann approximate Riemann solver. This solver is extended from the classical method developed in [9] and according to the principles developed in [10].

To capture with accuracy all the discontinuities that may arise into the solution, we introduce a third wave into the HLL solver. According to the method detailed in [10], this third wave represents a possible contact discontinuity. In addition, we construct this discontinuity so that it also represents jumps within some of the first derivatives of the solution. The resulting solver is a two-intermediate-state Riemann solver, adapted to the HLSM reconstruction. We call this solver the 'Hermite-HLLC' Riemann solver.

DOI: 10.1002/fld

This article is organized as follows: we start in Section 2 by defining the finite-volume framework of the method. In Section 3, we detail the construction and implementation of the HLSM reconstruction, for 1D scalar and 1D extended Euler equations. The interpolation polynomial is initially defined for use on irregular meshes; the specific procedure to generate a monotone reconstruction is then emphasized. In Section 4, we develop the specificities of the Hermite-HLLC Riemann solver that uses the HLSM interpolator.

Section 5 is devoted to numerical validations of the method.

First, to have a good understanding of the capabilities of the resulting method, we use a linear spectral analysis. According to the magnitude of the data-depending weights, this analysis gives us the salient features of the method in terms of stability range, behaviour of the 'spurious solution' and magnitude of the phase and amplitude errors. Technical details concerning this spectral analysis are given in Appendix A.

Then, we present numerical tests. These tests are selected to check the correct capture of discontinuities and especially of contact discontinuities. These tests also permit to compute realistic aeroacoustic problems with embedded discontinuities, without sacrificing accuracy.

Section 6 ends this work by giving some concluding remarks and drawing some perspectives for the future.

This work only concerns 1D results. Extension to multi-dimensional geometries is a substantial work and will be investigated in a future article.

2. GOVERNING EQUATIONS AND FINITE-VOLUME FRAMEWORK

2.1. Governing equations

Let the following scalar nonlinear hyperbolic problem be defined over the domain, Ω:

$$\begin{aligned} &u_t + f(u)_x = 0 \quad \forall x \in \Omega \\ &u(x, t=0) = u_0(x) \end{aligned} \tag{1}$$

Let $r \equiv u_x$ and $g(u,r) \equiv f'(u) \times u_x = f'(u) \times r$.

Let us suppose the smoothness of the initial solution, $u_0(x)$; then, by deriving (1), we can define the new nonlinear extended hyperbolic problem over Ω:

$$\begin{aligned} u_t + f(u)_x = 0, \quad u(x, t=0) = u_0(x) \\ r_t + g(u,r)_x = 0, \quad r(x, t=0) = u_0'(x) \end{aligned} \tag{2}$$

Note that, if the initial solution, $u_0(x)$, presents a singularity, then the extended system (2) can be derived from (1) by using the newly developed theory of 'delta-shock waves' (see [11] for more details); however, this possibility will not be investigated in this work. Since $g(u,r) = f'(u) \times r$, this implies that the characteristic velocity, $\partial g / \partial r$, of the equation for the derivative variables, r, is $f'(u)$. Consequently, both equations constituting (2) share the same characteristic velocity: this result is used in what follows to generate a simple approximate Riemann solver discretizing (2).

Defining the discrete cell $I_i \equiv [x_{i-1/2}, x_{i+1/2}]$, Ω is partitioned in N non-overlapping cells: $\Omega = \bigcup_{i=1}^{N} I_i$. The non-uniform cell size will be typified by: $\Delta x_i \equiv x_{i+1/2} - x_{i-1/2}$ or $\Delta x_{i+1/2} \equiv x_{i+1} - x_i$.

DOI: 10.1002/fld

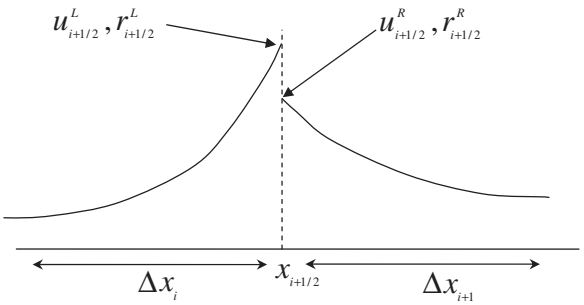

Figure 1. Reconstruction of the point values from cell averages at the interface $x = x_{i+1/2}$.

Finally, we define the discrete cell averages of $u(x,t)$ and $r(x,t)$ as: $\overline{u}_i(t) \equiv (1/\Delta x_i)\int_{I_i} u(x,t)\,\mathrm{d}x$, $\overline{r}_i(t) \equiv (1/\Delta x_i)\int_{I_i} r(x,t)\,\mathrm{d}x$. These cell averages are located at $x = x_i$, namely, the centre of the discrete cell, I_i, and $x_{i\pm1/2}$ represents the coordinates of the mesh.

Integrating (2) over I_i produces the following system of ordinary differential equations (ODE) for the variables $\overline{u}_i, \overline{r}_i$:

$$\begin{aligned}\frac{\mathrm{d}\overline{u}_i}{\mathrm{d}t} &= -\frac{1}{\Delta x_i}[f(u(x_{i+1/2},t)) - f(u(x_{i-1/2},t))]\\ \frac{\mathrm{d}\overline{r}_i}{\mathrm{d}t} &= -\frac{1}{\Delta x_i}[g(u(x_{i+1/2},t), r(x_{i+1/2},t)) - g(u(x_{i-1/2},t), r(x_{i-1/2},t))]\end{aligned} \tag{3}$$

By using the classical 'method of lines', time and space are separately discretized.

2.2. *Spatial approximation: the numerical fluxes*

Following the finite-volume methodology for generating a numerical scheme, the fluxes for u and r are approximated according to

$$\begin{aligned} f(u(x_{i+1/2},t)) &\approx \tilde{f}_{i+1/2} \equiv \tilde{f}(u^{\mathrm{l}}_{i+1/2}, u^{\mathrm{r}}_{i+1/2})\\ g(u(x_{i+1/2},t), r(x_{i+1/2},t)) &\approx \tilde{g}_{i+1/2} \equiv \tilde{g}(u^{\mathrm{l}}_{i+1/2}, r^{\mathrm{l}}_{i+1/2}, u^{\mathrm{r}}_{i+1/2}, r^{\mathrm{r}}_{i+1/2})\end{aligned} \tag{4}$$

$u^{\mathrm{l,r}}_{i+1/2}$ (resp. $r^{\mathrm{l,r}}_{i+1/2}$) represent the numerical approximations to the point values $u(x_{i+1/2},t_n)$ (resp. $r(x_{i+1/2},t_n)$), Figure 1. The manner of constructing the numerical fluxes, $\tilde{f}$, $\tilde{g}$, defines the upwind method.

To calculate these numerical fluxes, we selected the HLLE (Harten, Lax and Van-Leer) approximate Riemann solver [9].

Thus, we get the following expressions for the numerical fluxes $\tilde{f}$ and $\tilde{g}$:

$$\begin{aligned}\tilde{f}_{i+1/2} &= \frac{\lambda^+_{i+1/2} f(u^{\mathrm{l}}_{i+1/2}) - \lambda^-_{i+1/2} f(u^{\mathrm{r}}_{i+1/2})}{\lambda^+_{i+1/2} - \lambda^-_{i+1/2}} + \frac{\lambda^+_{i+1/2} \times \lambda^-_{i+1/2}}{\lambda^+_{i+1/2} - \lambda^-_{i+1/2}}(u^{\mathrm{r}}_{i+1/2} - u^{\mathrm{l}}_{i+1/2})\\ \tilde{g}_{i+1/2} &= \frac{\lambda^+_{i+1/2} g(u^{\mathrm{l}}_{i+1/2}, v^{\mathrm{l}}_{i+1/2}) - \lambda^-_{i+1/2} g(u^{\mathrm{r}}_{i+1/2}, v^{\mathrm{r}}_{i+1/2})}{\lambda^+_{i+1/2} - \lambda^-_{i+1/2}} + \frac{\lambda^+_{i+1/2} \times \lambda^-_{i+1/2}}{\lambda^+_{i+1/2} - \lambda^-_{i+1/2}}(v^{\mathrm{r}}_{i+1/2} - v^{\mathrm{l}}_{i+1/2})\end{aligned} \tag{5}$$

DOI: 10.1002/fld

In the scalar case, the following choices for the characteristic velocities $\lambda^{\pm}_{i+1/2}$ are:

$$\begin{aligned}\lambda^{+}_{i+1/2} &\equiv \max(f'(u^{\mathrm{l}}_{i+1/2}), f'(u^{\mathrm{r}}_{i+1/2}), a_{i+1/2}, 0)\\ \lambda^{-}_{i+1/2} &\equiv \min(f'(u^{\mathrm{l}}_{i+1/2}), f'(u^{\mathrm{r}}_{i+1/2}), a_{i+1/2}, 0)\end{aligned} \tag{6}$$

With

$$a_{i+1/2} \equiv \begin{cases} (f(u^{\mathrm{r}}_{i+1/2}) - f(u^{\mathrm{l}}_{i+1/2}))/(u^{\mathrm{r}}_{i+1/2} - u^{\mathrm{l}}_{i+1/2}) & \text{if } u^{\mathrm{r}}_{i+1/2} \neq u^{\mathrm{l}}_{i+1/2} \\ f'(u^{\mathrm{l}}_{i+1/2}) & \text{otherwise} \end{cases} \tag{7}$$

2.3. Time-integration scheme: the RGK3-TVD scheme

The discretization of the spatial operator generates an algebraic system of ODEs in time, for the discrete unknowns $(\overline{u}_i, \overline{r}_i)$.

If we define the following spatial operators:

$$\begin{aligned}F(\overline{u}, \overline{r})|_i &\equiv -\frac{1}{\Delta x_i}[\tilde{f}_{i+1/2} - \tilde{f}_{i-1/2}]\\ G(\overline{u}, \overline{r})|_i &\equiv -\frac{1}{\Delta x_i}[\tilde{g}_{i+1/2} - \tilde{g}_{i-1/2}]\end{aligned} \tag{8}$$

then, we obtain the following system of ODEs:

$$\begin{aligned}\frac{\mathrm{d}\overline{u}_i}{\mathrm{d}t} &= F(\overline{u}, \overline{r})|_i\\ \frac{\mathrm{d}\overline{r}_i}{\mathrm{d}t} &= G(\overline{u}, \overline{r})|_i\end{aligned} \tag{9}$$

This system is integrated by a third-order TVD Runge–Kutta scheme [12].

The general algorithm is

$$\begin{aligned}\phi^{(1)}_i &= \phi^n_i + \Delta t \times L(\phi^n)\\ \phi^{(2)}_i &= \frac{3}{4}\phi^n_i + \frac{1}{4}\phi^{(1)}_i + \frac{\Delta t}{4} \times L(\phi^{(1)})\\ \phi^{n+1}_i &= \frac{1}{3}\phi^n_i + \frac{2}{3}\phi^{(2)}_i + \frac{2\Delta t}{3} \times L(\phi^{(2)})\end{aligned} \tag{10}$$

with the following associated definitions:

$$\phi \equiv \begin{cases} \overline{u} \\ \overline{r} \end{cases} \quad \text{and} \quad L \equiv \begin{cases} F(\overline{u}, \overline{r}) \\ G(\overline{u}, \overline{r}) \end{cases}$$

DOI: 10.1002/fld

3. HLSM RECONSTRUCTION

In this section, we partly use notations introduced by Ollivier–Gooch in [7].

3.1. Least-square reconstruction from cell averages $(\overline{u}_i, \overline{r}_i)$

To begin with, we select an optimal Hermite polynomial of degree 4, denoted by $u_{\text{opt}}(x)$ and defined on the three-points stencil $\{I_{i-1}, I_i, I_{i+1}\}$, Figure 2: $u_{\text{opt}}(x) \equiv \sum_{j=0}^{4} a_j (x - x_i)^j$.

Then, using the definition of $\overline{u}_i$, located at the centre, $x = x_i$, of I_i

$$\overline{u}_i \equiv \frac{1}{\Delta x_i} \int_{I_i} u_{\text{opt}}(x)\, \mathrm{d}x = \frac{1}{\Delta x_i} \sum_{j=0}^{4} a_j \int_{I_i} (x - x_i)^j \, \mathrm{d}x \tag{11}$$

and introducing the practical notation

$$x_i^n \equiv \frac{1}{\Delta x_i} \int_{I_i} (x - x_i)^n \, \mathrm{d}x \tag{12}$$

We obtain the following result:

$$u_{\text{opt}}(x) - \overline{u}_i = \sum_{j=1}^{4} a_j [(x - x_i)^j - x_i^j] \tag{13}$$

And, consequently

$$\frac{1}{\Delta x_j} \int_{I_j} (u_{\text{opt}}(x) - \overline{u}_i)\, \mathrm{d}x \equiv \overline{u}_j - \overline{u}_i = a_1 \hat{x}_{ij}^1 + a_2 \hat{x}_{ij}^2 + a_3 \hat{x}_{ij}^3 + a_4 \hat{x}_{ij}^4, \quad j \in \{i-1, i+1\} \tag{14}$$

where we defined

$$\hat{x}_{ij}^n \equiv \frac{1}{\Delta x_j} \int_{I_j} [(x - x_i)^n - x_i^n] \, \mathrm{d}x, \quad j \in \{i-1, i+1\} \tag{15}$$

Therefore, we get the first useful algebraic relation defining the Hermite reconstruction

$$\overline{u}_j - \overline{u}_i = \sum_{n=1}^{4} a_n \hat{x}_{ij}^n, \quad j \in \{i-1, i+1\} \tag{16}$$

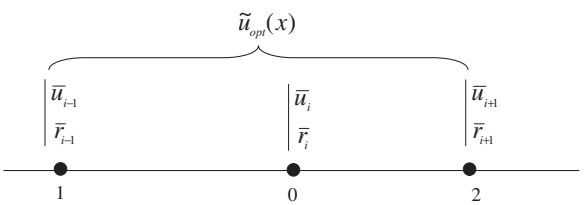

Figure 2. Central, left, and right stencils for the HCWENO6 procedure.

DOI: 10.1002/fld

The $\hat{x}_{ij}^n$ terms are terms that only depend on the mesh. Using the definition (12), these terms can be developed to give the following results:

$$\begin{aligned}
\hat{x}_{ij}^1 &= (x_j - x_i) \\
\hat{x}_{ij}^2 &= (x_j - x_i)^2 + \frac{1}{12}(\Delta x_j^2 - \Delta x_i^2) \\
\hat{x}_{ij}^3 &= (x_j - x_i)^3 + \frac{\Delta x_j^2}{4}(x_j - x_i) \qquad j \in \{i-1, i+1\} \\
\hat{x}_{ij}^4 &= (x_j - x_i)^4 + \frac{\Delta x_j^2}{2}(x_j - x_i)^2 + \frac{1}{80}(\Delta x_j^4 - \Delta x_i^4)
\end{aligned} \tag{17}$$

Practically, these terms are pre-computed and stored in the computer memory.

Now, by defining $r_{\text{opt}}(x) \equiv \mathrm{d}u_{\text{opt}}(x)/\mathrm{d}x$ and by following the same procedure as for $u_{\text{opt}}(x)$, we obtain the second useful algebraic relation

$$\overline{r}_j - \overline{r}_i = \sum_{n=2}^{4} n a_n \hat{x}_{ij}^{n-1}, \quad j \in \{i-1, i+1\} \tag{18}$$

Then, gathering (16) and (18), we obtain the following algebraic system:

$$\begin{bmatrix} L_{i1} \\ L_{i2} \\ L_{i3} \\ L_{i4} \end{bmatrix} \times \begin{pmatrix} a_1 \\ a_2 \\ a_3 \\ a_4 \end{pmatrix}_i = \begin{pmatrix} \overline{u}_{i-1} - \overline{u}_i \\ \overline{u}_{i+1} - \overline{u}_i \\ \overline{r}_{i-1} - \overline{r}_i \\ \overline{r}_{i+1} - \overline{r}_i \end{pmatrix} \tag{19}$$

with

$$\begin{aligned}
L_{i1,2} &\equiv [\hat{x}_{ij}^1, \hat{x}_{ij}^2, \hat{x}_{ij}^3, \hat{x}_{ij}^4]^t \\
L_{i3,4} &\equiv [0, 2\hat{x}_{ij}^1, 3\hat{x}_{ij}^2, 4\hat{x}_{ij}^3]^t
\end{aligned} \qquad j \in \{i-1, i+1\} \tag{20}$$

At this step, system (19) is a 4×4 system and it generates a fifth-order oscillatory reconstruction.

To introduce monotonicity into the calculation of the derivatives, $\{a_j\}$, let us define over the cell I_i, a low-order monotone polynomial, namely: $u_{\text{M}}(x)$.

This polynomial is defined by a TVD principle. Then, this polynomial is used in order to produce two supplementary equations:

$$\begin{aligned}
\frac{1}{\Delta x_{i-1/2}} \int_{x_{i-1}}^{x_i} u_{\text{opt}}(x)\,\mathrm{d}x &= \frac{1}{\Delta x_{i-1/2}} \int_{x_{i-1}}^{x_i} u_{\text{M}}(x)\,\mathrm{d}x \\
\frac{1}{\Delta x_{i+1/2}} \int_{x_i}^{x_{i+1}} u_{\text{opt}}(x)\,\mathrm{d}x &= \frac{1}{\Delta x_{i+1/2}} \int_{x_i}^{x_{i+1}} u_{\text{M}}(x)\,\mathrm{d}x
\end{aligned} \tag{21}$$

DOI: 10.1002/fld

In other words, the high-order polynomial, $u_{\mathrm{opt}}(x)$, must locally coincide, *in average*, with the monotone low-order polynomial, $u_{\mathrm{M}}(x)$. Using the definition of $u_{\mathrm{opt}}(x)$ and developing the left-hand side of (21), one obtains two supplementary algebraic conditions for the $\{a_j\}$

$$\begin{aligned} -a_1\frac{\Delta x_{i-1/2}}{2}+a_2\frac{\Delta x_{i-1/2}^2}{4}-a_3\frac{\Delta x_{i-1/2}^3}{4}+3a_4\frac{\Delta x_{i-1/2}^4}{16} &= \frac{1}{\Delta x_{i-1/2}}\int_{x_{i-1}}^{x_i} u_{\mathrm{M}}(x)\,\mathrm{d}x-\overline{u}_i \\ a_1\frac{\Delta x_{i+1/2}}{2}+a_2\frac{\Delta x_{i+1/2}^2}{4}+a_3\frac{\Delta x_{i+1/2}^3}{4}+3a_4\frac{\Delta x_{i+1/2}^4}{16} &= \frac{1}{\Delta x_{i+1/2}}\int_{x_i}^{x_{i+1}} u_{\mathrm{M}}(x)\,\mathrm{d}x-\overline{u}_i \end{aligned} \tag{22}$$

These two relations are re-interpreted as monotonicity constraints to be added to system (19) in order to generate a monotone reconstruction. Consequently, we obtain the following 6×4 system:

$$\begin{bmatrix} L_{i1} \\ L_{i2} \\ L_{i3} \\ L_{i4} \\ L_{i5} \\ L_{i6} \end{bmatrix} \times \begin{pmatrix} \tilde{a}_1 \\ \tilde{a}_2 \\ \tilde{a}_3 \\ \tilde{a}_4 \end{pmatrix}_i = \begin{pmatrix} \overline{u}_{i-1}-\overline{u}_i \\ \overline{u}_{i+1}-\overline{u}_i \\ \overline{r}_{i-1}-\overline{r}_i \\ \overline{r}_{i+1}-\overline{r}_i \\ B_5 \\ B_6 \end{pmatrix} \tag{23}$$

with

$$\begin{aligned} L_{i5} &\equiv \left[-\frac{\Delta x_{i-1/2}}{2}, \frac{\Delta x_{i-1/2}^2}{4}, -\frac{\Delta x_{i-1/2}^3}{4}, 3\frac{\Delta x_{i-1/2}^4}{16}\right]^{\mathrm{t}} \\ L_{i6} &\equiv \left[\frac{\Delta x_{i+1/2}}{2}, \frac{\Delta x_{i+1/2}^2}{4}, \frac{\Delta x_{i+1/2}^3}{4}, 3\frac{\Delta x_{i+1/2}^4}{16}\right]^{\mathrm{t}} \end{aligned} \tag{24}$$

and

$$\begin{aligned} B_5 &\equiv \frac{1}{\Delta x_{i-1/2}}\int_{x_{i-1}}^{x_i} u_M(x)\,\mathrm{d}x-\overline{u}_i \\ B_6 &\equiv \frac{1}{\Delta x_{i+1/2}}\int_{x_i}^{x_{i+1}} u_M(x)\,\mathrm{d}x-\overline{u}_i \end{aligned} \tag{25}$$

In this manner, it becomes possible to introduce a monotonicity principle in the calculation of the new polynomial coefficients, $\{\tilde{a}_j\}$.

However, the monotonicity principle introduced by (21) is only desirable when the solution is discontinuous or when it exists strong gradients; in regions of smoothness, constraints (21) must be relaxed to obtain the best accuracy for the reconstruction. This process is ensured by the introduction of a data-depending weight, w_i, into (23).

DOI: 10.1002/fld

3.2. Weighting of the monotonicity constraints

The principles we adopted for calculating the data-depending weight, w_i, are as follows:

- w_i must smoothly vary between a very small value, in regions of smoothness, and a value $O(1)$ at the location of a discontinuity.
- In regions of smoothness, the modification introduced by w_i must not generate a term that would be greater than the spatial truncature error of the scheme.

To begin, we calculate the general indicator of smoothness over the cell I_i [4] as

$$\mathrm{IS}_i \equiv \frac{1}{u_{\max}^2} \sum_{k=1}^{4} \Delta x_i^{2k-1} \times \int_{I_i} \left(\frac{\mathrm{d}^k u_{\mathrm{opt}}}{\mathrm{d}x^k} \right)^2 \mathrm{d}x \tag{26}$$

where $u_{\max}$ is calculated over the whole calculation domain Ω: $u_{\max} = \max_{x\in\Omega} |u|$. This indicator provides a measure of the smoothness of the solution over the cell I_i, according to the stencil selected to define $u_{\mathrm{opt}}(x)$ on that cell. In regions of smoothness, $\mathrm{IS}_i \ll 1$, whereas $\mathrm{IS}_i = O(1)$ in cells with strong gradients or discontinuities.

According to the definition of $u_{\mathrm{opt}}(x)$, formula (26) can be developed to yield

$$\mathrm{IS}_i = a_1^2 \Delta x_i^2 + (\tfrac{13}{3} a_2^2 + \tfrac{1}{2} a_1 a_3) \Delta x_i^4 + (\tfrac{21}{5} a_2 a_4 + \tfrac{3129}{80} a_3^2) \Delta x_i^6 \tag{27}$$

This formula is valid even on non-uniform meshes. In this formula, the $\{a_j\}$ are the polynomial coefficients of $u_{\mathrm{opt}}(x)$ and are solutions of system (19).

Since system (19) is a 4×4 system of which the coefficients are only metric terms, *it is inverted once*, at the beginning of the computations, by a direct method; the result is then stored in the computer memory. Therefore, it only remains to calculate IS_i, at each time step, by (27). When the mesh is uniform or smoothly varying ($\Delta x_i = \Delta x \approx \mathrm{Cte}$), the coefficients $\{a_j\}$ can be simply formulated to give the relations that follow:

$$\begin{aligned}
\Delta x \times a_1 &= \frac{27}{64}(\overline{u}_{i-1} - \overline{u}_{i+1}) + \Delta x \left[\frac{19}{192}(\overline{r}_{i+1} + \overline{r}_{i-1}) + \frac{79}{48}\overline{r}_i \right] \\
\Delta x^2 \times a_2 &= \frac{5}{4}(\overline{u}_{i+1} - 2\overline{u}_i + \overline{u}_{i-1}) + \frac{3\Delta x}{8}(\overline{r}_{i-1} - \overline{r}_{i+1}) \\
\Delta x^3 \times a_3 &= \frac{45}{24}(\overline{u}_{i+1} - \overline{u}_{i-1}) - \frac{\Delta x}{24}[11(\overline{r}_{i+1} + \overline{r}_{i-1}) + 68\overline{r}_i] \\
\Delta x^4 \times a_4 &= -\frac{1}{2}(\overline{u}_{i+1} - 2\overline{u}_i + \overline{u}_{i-1}) + \frac{\Delta x}{4}(\overline{r}_{i+1} - \overline{r}_{i-1})
\end{aligned} \tag{28}$$

Remark 1

The coefficients $\{a_j\}$ and $\{\tilde{a}_j\}$ should not be confused in the formulae above. The coefficients $\{a_j\}$ are solution of (19) and characterize the high-order oscillatory polynomial, $u_{\mathrm{opt}}(x)$. The coefficients $\{\tilde{a}_j\}$ are the solution of (23) and represent the modified version of $u_{\mathrm{opt}}(x)$ to obtain a monotone reconstruction; henceforth, this resulting polynomial will be noted as, $\tilde{u}_{\mathrm{opt}}(x)$.

Remark 2

Numerical experiments that follow showed us that only the coefficients $\{a_1, a_2\}$ (first and second derivatives of the numerical solution) are necessary to properly estimate IS_i: the most important

DOI: 10.1002/fld

point in the calculation of IS_i is to discriminate between a shock and a smooth extremum. However, in order not to compromise the generality of the method, we give the entire formula (27): the only drawback is in a slight increase of the computing time.

Having calculated the smoothness indicators, IS_i, for each cell I_i, now, we introduce a normalized smoothness indicator, namely β_i, defined on I_i and such that

$$\begin{aligned} &\beta_i \to 0 \quad \text{in regions of smoothness} \\ &\beta_i \to 1^- \quad \text{if there exist a discontinuity} \end{aligned} \tag{29}$$

Practically, we use the formulation experimented in [8]:

$$\beta_i \equiv \frac{(\mathrm{IS}_i)^2}{1+(\mathrm{IS}_i)^2} \quad \forall x \in I_i \tag{30}$$

This normalized smoothness indicator was selected in order to enhance the robustness of the method. Indeed, whatever the problem encountered, this sensor always varies in the interval [0, 1]; thus, it becomes easier to define a general procedure that adapts automatically to the solution, independently of the magnitude of the discrete variable, $\overline{u}_i$. In addition, this choice facilitates the calculation of the data-depending weight, w_i, and ensures that this weight introduces a correction that is less than the truncature error when the solution is smooth. This latter point will be checked in a section that follows.

When the mesh is uniform, one can verify that formula (30) follows the requirements of (29). Indeed, expanding (28) around $x = x_i$ ($\Delta x_i = \Delta x \equiv \mathrm{Cte}$) and introducing the result into (27), yields the following form:

$$\mathrm{IS}_i = (\Delta x \times u_x)_i^2 + \tfrac{13}{12}(\Delta x^2 u_{xx})_i^2 + O(\Delta x^5) \tag{31}$$

Therefore IS_i has the form

$$\mathrm{IS}_i = (\Delta x \times u_x)_i^2 (1 + C\Delta x^2)$$

Consequently, β_i is such that

$$\beta_i \approx \frac{(\Delta x \times u_x)_i^4}{1+(\Delta x \times u_x)_i^4} \tag{32}$$

Thus, $\beta_i = O(\Delta x^4)$ in regions of smoothness of the solution and approaches unity by its lower bound in cells crossed by a discontinuity.

Now, we can define the data-depending weight, w_i, that is devised to modulate conditions (22) into the linear system (23)

$$w_i \equiv \alpha \times \beta_i = \frac{\alpha \times \mathrm{IS}_i^2}{1+\mathrm{IS}_i^2} \tag{33}$$

where α represents an arbitrary parameter such that $\alpha = O(1)$. In what follows, α will be called the 'monotonicity parameter'.

Once w_i is defined, it can be introduced in (23) to weigh the monotonicity constraints (22).

DOI: 10.1002/fld

Thus, (23) is modified by the new quantities

$$\begin{aligned} \tilde{B}_{5,6} &\equiv w_i B_{5,6} \\ \tilde{L}_{i5,6} &\equiv w_i L_{i5,6} \end{aligned} \tag{34}$$

All the remaining components of (23) are left unchanged.

Remark 1
Of course, choice (33) is not unique: trial and errors are permitted to isolate this formulation. One could have chosen the solution employed in [8] that uses hyperbolic functions; however, this solution necessitates to define numerical thresholds to optimize its behaviour: this would lessen the generality of the method.

Remark 2
Considering the asymptotic behaviour of β_i, the use of parameter α is not strictly mandatory. However, as we shall see in numerical experiments, this parameter is useful in order to optimize the capture of a discontinuity. In this sense, α is equivalent to parameters introduced into limiters with TVD methods.

Now, to completely define the HLSM reconstruction, it is left to define the monotone polynomial, namely $u_{\mathrm{M}}(x)$.

3.3. Definition of the monotone polynomial, $u_{\mathrm{M}}(x)$: TVD monotonicity condition

To impose a TVD monotonicity constraint in (23), we select the simplest TVD limiter, known in the literature as the 'Minmod limiter'. Then, on a non-uniform mesh, $u_{\mathrm{M}}(x)$ is simply calculated according to the following formula:

$$u_{\mathrm{M}}(x) \equiv \overline{u}_i + (x - x_i) \times \min \text{ mod} \left(\frac{\overline{u}_{i+1} - \overline{u}_i}{\Delta x_{i+1/2}}, \frac{\overline{u}_i - \overline{u}_{i-1}}{\Delta x_{i-1/2}} \right) \quad \forall x \in I_i \tag{35}$$

Thus, according to (22), it becomes possible to formulate $\tilde{B}_{5,6}$ in (23)

$$\begin{aligned} \tilde{B}_5 &\equiv -w_i \frac{\Delta x_i}{2} \times \min \text{ mod} \left(\frac{\overline{u}_{i+1} - \overline{u}_i}{\Delta x_{i+1/2}}, \frac{\overline{u}_i - \overline{u}_{i-1}}{\Delta x_{i-1/2}} \right) \\ \tilde{B}_6 &\equiv w_i \frac{\Delta x_i}{2} \times \min \text{ mod} \left(\frac{\overline{u}_{i+1} - \overline{u}_i}{\Delta x_{i+1/2}}, \frac{\overline{u}_i - \overline{u}_{i-1}}{\Delta x_{i-1/2}} \right) \end{aligned} \tag{36}$$

The HLSM reconstruction that uses (36) as a monotonicity constraint for (23) will be referenced in what follows as the 'HLSM-Minmod' reconstruction.

Generally speaking, TVD schemes, independently of their particular form, are necessarily only first-order accurate at local extrema. Therefore, one can expect that this reconstruction will degenerate into a first-order method at discontinuities; this point will be checked in what follows.

3.4. Accuracy analysis

Up to this point, it is difficult to estimate, with accuracy, the theoretical monotonicity properties of the HLSM reconstruction; indeed, the coefficients $\{\tilde{a}_j\}$ defined in (23) are not easy to formulate, analytically.

DOI: 10.1002/fld

However, we can get an idea of the behaviour of the scheme if we reduce its scope.

To this aim, let us suppose that the mesh is uniform ($\Delta x_i = \Delta x \equiv \text{Cte}$) and that we calculate the polynomial coefficients, $\{\tilde{a}_j\}$, by a Gram–Schmidt process. Furthermore, we suppose that $\tilde{B}_{5,6} \equiv w_i \times B_{5,6}$ verify the following properties, in agreement with formula (36):

$$\tilde{B}_6 = -\tilde{B}_5 = \begin{cases} O(w_i \times \Delta x) = O(\Delta x^5) & \text{smooth data} \\ 0 & \text{non-smooth data} \end{cases} \tag{37}$$

In this manner, it becomes possible to determine the $\{\tilde{a}_j\}$ by using the MAPLE symbolic mathematical computer package.

To check the accuracy of the HLSM reconstruction, we simply study the discretization of $(u_x|_i, r_x|_i \equiv u_{xx}|_i)$. The weight, w_i, and the quantity, B_5, are selected as parameters for this study.

Having calculated the analytical expressions for the $\{\tilde{a}_j\}$, then it becomes possible to estimate the interpolated values, $(u^{\mathrm{I}}_{i+1/2}, r^{\mathrm{I}}_{i+1/2}) \equiv (\tilde{u}_{\mathrm{opt}}(x_{i+1/2}), \mathrm{d}\tilde{u}_{\mathrm{opt}}(x_{i+1/2})/\mathrm{d}x)$. Consequently, we can calculate the quantity $(u^{\mathrm{I}}_{i+1/2} - u^{\mathrm{I}}_{i-1/2})/\Delta x$ (respectively, $(r^{\mathrm{I}}_{i+1/2} - r^{\mathrm{I}}_{i-1/2})/\Delta x$) as an approximation of $u_x|_i$ (respectively, $u_{xx}|_i$). Doing this and keeping only the leading terms, we obtain the results that follow:

$$\begin{aligned} \frac{u^{\mathrm{I}}_{i+1/2} - u^{\mathrm{I}}_{i-1/2}}{\Delta x} &\sim \left[1 - \frac{B_5 \times w_i^2}{(w_i^2+4)}\right] \times u_x|_i + O(w_i^2 \Delta x) \\ \frac{r^{\mathrm{I}}_{i+1/2} - r^{\mathrm{I}}_{i-1/2}}{\Delta x} &\sim u_{xx}|_i + O(w_i^2 \Delta x) \end{aligned} \tag{38}$$

If the solution is continuous, then we have: $w_i = O(\alpha \times \Delta x^4)$ and $B_5 = O(\Delta x)$. Inserting those results into (38), we get the following approximations:

$$\begin{aligned} \frac{u^{\mathrm{I}}_{i+1/2} - u^{\mathrm{I}}_{i-1/2}}{\Delta x} &\sim u_x|_i + \frac{\Delta x^5}{360} u_{6x}|_i \\ \frac{r^{\mathrm{I}}_{i+1/2} - r^{\mathrm{I}}_{i-1/2}}{\Delta x} &\sim u_{xx}|_i + \frac{\Delta x^4}{120} u_{5x}|_i \end{aligned} \tag{39}$$

Therefore, the resulting discretization is fifth-order accurate for the variable, u, and fourth order for its first derivative, r. It is noteworthy that those results depend neither on the monotonicity parameter, α, nor of the value of B_5. This means that as long as the solution is smooth, the monotonicity constraints in the second member of (23) do not have any influence upon the spatial accuracy of the scheme.

Now, if the solution becomes discontinuous into the discrete cell, I_i, we have, by construction: $w_i = O(\alpha)$ and $B_5 = 0$. In such a case, by developing the $O(w_i^2 \times \Delta x)$ terms into formulae (38), we get the result that follows:

$$\begin{aligned} \frac{u^{\mathrm{I}}_{i+1/2} - u^{\mathrm{I}}_{i-1/2}}{\Delta x} &\sim u_x|_i - \frac{\alpha^2 \Delta x}{2(4+\alpha^2)} u_{xx}|_i + O(\Delta x^2) \\ \frac{r^{\mathrm{I}}_{i+1/2} - r^{\mathrm{I}}_{i-1/2}}{\Delta x} &\sim u_{xx}|_i + \frac{28\alpha^2 \Delta x}{(256+49\alpha^2)} u_{3x}|_i + O(\Delta x^2) \end{aligned} \tag{40}$$

DOI: 10.1002/fld

Therefore, at cells crossed by a discontinuity, the discretization of (u_x, u_{xx}) becomes first order. In this case the parameter, α, acts to modulate the dissipative term that prevents the appearance of non-physical oscillations. Concerning the variable, u, for example, this dissipative term can be compared with the one obtained via a first-order upwind discretization. Indeed, a first-order discretization of $u_x|_i$ produces the following truncature error:

$$\tfrac{1}{2}\Delta x \times u_{xx}|_i + O(\Delta x^2) \tag{41}$$

while the HLSM reconstruction generates the term:

$$\frac{\alpha^2 \Delta x}{2(4+\alpha^2)} u_{xx}|_i + O(\Delta x^2) \tag{42}$$

Comparing these results, we can see that the HLSM reconstruction gives a lower dissipative term, whatever the value of α. When α increases, the dissipation increases; however, in every case, this dissipative term remains bounded by the quantity given by (41) (upper bound).

Therefore, the HLSM scheme asymptotically tends towards a first-order scheme at the location of a discontinuity. Practically, the HLSM reconstruction results in a weighting between a fifth-order oscillatory interpolation and a first-order monotone approximation. This weighting does not deteriorate the accuracy for smooth data but produces a monotone behaviour when discontinuities are present into the solution.

Numerical experiments that follow will help to verify this behaviour, dynamically.

3.5. The HLSM upwind scheme for scalar hyperbolic problems

The final form of the HLSM upwind scheme is given by

$$\begin{aligned} \left.\frac{\partial f}{\partial x}\right|_i &= \frac{(\tilde{f}_{i+1/2} - \tilde{f}_{i-1/2})}{\Delta x_i} \\ \left.\frac{\partial g}{\partial x}\right|_i &= \frac{(\tilde{g}_{i+1/2} - \tilde{g}_{i-1/2})}{\Delta x_i} \end{aligned} \tag{43}$$

and

$$\begin{aligned} u^1_{i+1/2} &= \tilde{u}_{\mathrm{opt}}(x_{i+1/2}) = \overline{u}_i + \tilde{a}_1 \frac{\Delta x_i}{2} + \tilde{a}_2 \frac{\Delta x_i^2}{6} + \tilde{a}_3 \frac{\Delta x_i^3}{8} + \tilde{a}_4 \frac{\Delta x_i^4}{20} \\ r^1_{i+1/2} &= \frac{\mathrm{d}}{\mathrm{d}x} \tilde{u}_{\mathrm{opt}}(x_{i+1/2}) = \overline{r}_i + \tilde{a}_2 \Delta x_i + \tilde{a}_3 \frac{\Delta x_i^2}{2} + \tilde{a}_4 \frac{\Delta x_i^3}{2} \end{aligned} \tag{44}$$

$\tilde{f}_{i+1/2}$ and $\tilde{g}_{i+1/2}$ are calculated by the HLLE solver (formulae (5)–(7)). To calculate $\tilde{u}_{\mathrm{opt}}(x)$, over I_i, system (23) with modification (34) is inverted. The data-depending weight, w_i, is calculated according to (33) and the monotone polynomial, $u_{\mathrm{M}}(x)$, that defines $\tilde{B}_{5,6}$ is calculated by introducing the TVD-monotonicity constraint (formula (36)).

The result is a polynomial, $\tilde{u}_{\mathrm{opt}}(x)$, locally defined over the cell I_i, and devised to be non-oscillatory, *in the mean* (conditions (21)). The resulting scheme is spatially fifth-order accurate in smooth regions of the solution and tends towards a first-order accuracy in regions crossed by a discontinuity.

DOI: 10.1002/fld

Remark
Practically, system (23) is inverted by using Householder transforms to reduce the left-hand side of (23) to upper-triangular form. When the cell aspect ratio becomes very large, one can note some conditioning problems if one uses normal equations to solve the least-square problem. Householder transforms are much less sensitive to the matrix condition number [5]; this implies a greater robustness of the resulting method.

4. HLL RIEMANN SOLVER FOR THE EXTENDED EULER EQUATION

In this section, we extend the HLSM scheme to solve systems of hyperbolic conservation laws and we develop a specific HLL Riemann solver, namely the 'Hermite-HLLC' Riemann solver. Specifically, we consider the 1D Euler equations in the following conservation form:

$$\frac{\partial U}{\partial t}+\frac{\partial f(U)}{\partial x}=0 \tag{45}$$

where

$$U\equiv[\rho,\rho u,e]^{\mathrm{t}},\quad f\equiv[\rho u,\rho u^2+p,\rho uH]^{\mathrm{t}} \tag{46}$$

$H\equiv(e+p)/\rho$ is the specific total enthalpy and this set of equations is closed by the equation-of-state of an ideal gas: $p=(\gamma-1)(e-\rho u^2/2),\gamma=1.40$.

In order to use a Hermite procedure, we derive the following set of systems from (45):

$$\begin{aligned}\frac{\partial U}{\partial t}+\frac{\partial f(U)}{\partial x}&=0\\ \frac{\partial V}{\partial t}+\frac{\partial g(U,V)}{\partial x}&=0\end{aligned} \tag{47}$$

where we defined: $V\equiv[(\rho)_x,(\rho u)_x,e_x]^{\mathrm{t}}, g\equiv[(\rho u)_x,(\rho u^2+p)_x,(\rho uH)_x]^{\mathrm{t}}$.

Defining the Jacobian matrix, $A\equiv\partial f/\partial U$, we get the following property for the flux g: $g\equiv f_x=A(U)\times V$.

This system constitutes the extended form of the 1D Euler equations. In a more condensed form, (47) can be equivalently written as

$$\begin{aligned}\tilde{U}_{\mathrm{t}}+F(\tilde{U})_x&=0\\ \tilde{U}\equiv[U,V]^{\mathrm{t}};\quad F&\equiv[f,g]^{\mathrm{t}}\end{aligned} \tag{48}$$

To be able to calculate possible discontinuities within the solution of (48), we need to discriminate between a contact discontinuity and a shock wave. For this reason, we adapt the so-called 'HLLC Riemann solver', devised in [10], to our problem: this scheme will be called in what follows, as the 'Hermite-HLLC' scheme.

The henceforth classical HLLE Riemann solver has many advantages: it automatically satisfies an entropy condition, captures isolated shocks and preserves positivity [9]. However, it is unable to exactly capture isolated contact discontinuities.

The HLLC Riemann solver, initially elaborated by Toro *et al.* [10], suppresses this drawback. It is a two-state HLL approximation that introduces the contribution of a contact discontinuity.

The solution we propose is an extended version of the HLLC scheme for weakly hyperbolic systems of conservation laws.

DOI: 10.1002/fld

To begin with, let us consider two-averaged intermediate states, $\tilde{U}_{\mathrm{l}}^{*}$ and $\tilde{U}_{\mathrm{r}}^{*}$, separated by a contact discontinuity, of which speed is denoted by λ^{m}.

Defining this contact wave, we get the first relations for the variable U:

$$\lambda^{\mathrm{m}} \equiv u^{\mathrm{m}} = u_{\mathrm{l}}^{*} = u_{\mathrm{r}}^{*} \tag{49a}$$

Then, using the Rankine–Hugoniot conditions for U, we deduce that

$$p_{\mathrm{l}}^{*} = p_{\mathrm{r}}^{*} \equiv p^{\mathrm{m}} \tag{49b}$$

Relations (49a) and (49b) entirely define the contact discontinuity, for the variable U.

Now, let us calculate the relations verified by the variable V, for this same discontinuity. To do these calculations, we made the significant assumption that *the contact discontinuity in U generates also a discontinuity in V that propagates at the same velocity*.

Then, the Rankine–Hugoniot relations verified by the variable V, for a discontinuity propagating at the velocity, u^{m}, are as follows (the '*' are temporarily omitted, for simplicity):

$$\begin{aligned} (\rho u)_x^{\mathrm{l}} - (\rho u)_x^{\mathrm{r}} &= u^{\mathrm{m}}(\rho_x^{\mathrm{l}} - \rho_x^{\mathrm{r}}) \\ (\rho u^2 + p)_x^{\mathrm{l}} - (\rho u^2 + p)_x^{\mathrm{r}} &= u^{\mathrm{m}}((\rho u)_x^{\mathrm{l}} - (\rho u)_x^{\mathrm{r}}) \\ \{u(e+p)\}_x^{\mathrm{l}} - \{u(e+p)\}_x^{\mathrm{r}} &= u^{\mathrm{m}}(e_x^{\mathrm{l}} - e_x^{\mathrm{r}}) \end{aligned} \tag{50}$$

Using (49a) into the first equation of (50), yields the first result verified across the contact wave in V:

$$[\rho u_x] = 0 \tag{51a}$$

Then, using this result with (49a) and (49b) within the second equation of (50), we obtain the second useful relation

$$[p_x] = 0 \tag{51b}$$

Finally, inserting these results into the last equation of (50), this equation is identically verified.

Therefore, the contact discontinuity that propagates at the speed u^{m}, is typified by the following relations across this wave:

$$\begin{aligned} [u] = [p] &= 0 \\ [\rho u_x] = [p_x] &= 0 \end{aligned} \tag{52}$$

Now, we are able to completely calculate the intermediate states, $\tilde{U}_{\mathrm{l}}^{*}$ and $\tilde{U}_{\mathrm{r}}^{*}$, by using those results.

First, we calculate the intermediate states for the vectors U_{l}^{*} and U_{r}^{*}: this calculation is detailed in [10, 13] and will not be repeated, here; we only give the results we need to calculate V_{l}^{*} and V_{r}^{*}.

Thus, we get the following results from [10]:

$$u^{\mathrm{m}} = \frac{\rho^{\mathrm{r}} u^{\mathrm{r}}(\lambda^{\mathrm{r}} - u^{\mathrm{r}}) - \rho^{\mathrm{l}} u^{\mathrm{l}}(\lambda^{\mathrm{l}} - u^{\mathrm{l}}) + p^{\mathrm{l}} - p^{\mathrm{r}}}{\rho^{\mathrm{r}}(\lambda^{\mathrm{r}} - u^{\mathrm{r}}) - \rho^{\mathrm{l}}(\lambda^{\mathrm{l}} - u^{\mathrm{l}})} \tag{53a}$$

$$\rho_{\mathrm{l,r}}^{*} = \rho^{\mathrm{l,r}} \frac{(\lambda^{\mathrm{l,r}} - u^{\mathrm{l,r}})}{\lambda^{\mathrm{l,r}} - u^{\mathrm{m}}} \tag{53b}$$

DOI: 10.1002/fld

$$p^{\mathrm{m}} = p^{\mathrm{l}} + \rho^{\mathrm{l}}(u^{\mathrm{l}} - u^{\mathrm{m}}) \times (u^{\mathrm{l}} - \lambda^{\mathrm{l}}) \tag{53c}$$

$$e^{*}_{\mathrm{l,r}} = \frac{e^{\mathrm{l,r}}(\lambda^{\mathrm{l,r}} - u^{\mathrm{l,r}}) - p^{\mathrm{l,r}}u^{\mathrm{l,r}} + p^{\mathrm{m}}u^{\mathrm{m}}}{\lambda^{\mathrm{l,r}} - u^{\mathrm{m}}} \tag{53d}$$

These results make it possible to calculate the intermediate states, U^{*}_{l} and U^{*}_{r}.

Now, we utilize those results to calculate V^{*}_{l} and V^{*}_{r}. Writing the Rankine–Hugoniot conditions, for the variable V, across the left wave, λ^{l}, that connects the state V^{*}_{l} with V_{l}, we obtain the relations

$$g^{\mathrm{l}}_{1} \equiv (\rho u)_x|^{*}_{\mathrm{l}} - \lambda^{\mathrm{l}}\rho_x|^{*}_{\mathrm{l}} = (\rho u)^{\mathrm{l}}_x - \lambda^{\mathrm{l}}\rho^{\mathrm{l}}_x \tag{54a}$$

$$g^{\mathrm{l}}_{2} \equiv (\rho u^2 + p)_x|^{*}_{\mathrm{l}} - \lambda^{\mathrm{l}}(\rho u)_x|^{*}_{\mathrm{l}} = (\rho u^2 + p)^{\mathrm{l}}_x - \lambda^{\mathrm{l}}(\rho u)^{\mathrm{l}}_x \tag{54b}$$

$$g^{\mathrm{l}}_{3} \equiv \{u(e+p)\}_x|^{*}_{\mathrm{l}} - \lambda^{\mathrm{l}}e_x|^{*}_{\mathrm{l}} = \{u(e+p)\}^{\mathrm{l}}_x - \lambda^{\mathrm{l}}e^{\mathrm{l}}_x \tag{54c}$$

Identical relations are obtained across the right wave, λ^{r}, that connects the state V^{*}_{r} with V_{r}.

Then, using $[u]=0$ in (54a), we get the first equation

$$\rho_x|^{*}_{\mathrm{l,r}} = \frac{g^{\mathrm{l,r}}_{1} - (\rho u_x)^{\mathrm{m}}}{u^{\mathrm{m}} - \lambda^{\mathrm{l,r}}} \tag{55a}$$

Introducing this result into (54b) and using $[u]=[p_x]=0$, we obtain

$$(\rho u_x)^{\mathrm{m}} = \frac{g^{\mathrm{r}}_{2} - g^{\mathrm{l}}_{2} + u^{\mathrm{m}}(g^{\mathrm{l}}_{1} - g^{\mathrm{r}}_{1})}{\lambda^{\mathrm{l}} - \lambda^{\mathrm{r}}} \tag{55b}$$

Re-introducing (55b) into (54b), yields

$$p^{\mathrm{m}}_x = g^{\mathrm{l}}_{2} + u^{\mathrm{m}}(\lambda^{\mathrm{l}} - u^{\mathrm{m}}) \times \rho_x|^{*}_{\mathrm{l}} + (\lambda^{\mathrm{l}} - 2u^{\mathrm{m}}) \times (\rho u_x)^{\mathrm{m}} \tag{55c}$$

Finally, using those results in (54c), yields

$$e_x|^{*}_{\mathrm{l,r}} = \frac{\{g^{\mathrm{l,r}}_{3} - u_x(e+p)|^{*}_{\mathrm{l,r}} - u^{\mathrm{m}}p^{\mathrm{m}}_x\}}{(u^{\mathrm{m}} - \lambda^{\mathrm{l,r}})} \tag{55d}$$

All the remaining variables can be deduced from the relations, above.

Therefore, relations (53) and (55) permit to calculate $\tilde{U}^{*}_{\mathrm{l}}$ and $\tilde{U}^{*}_{\mathrm{r}}$, knowing $\tilde{U}_{\mathrm{l}}$ and $\tilde{U}_{\mathrm{r}}$. Now, we can formulate the algorithm that defines the HLLC scheme for the extended Euler equations.

The two-state approximate Riemann solution given by the Hermite-HLLC scheme is the following one:

$$\tilde{U}_{i+1/2} = \begin{cases} \tilde{U}^{\mathrm{l}} & \text{if } \lambda^{\mathrm{l}} > 0 \\ \tilde{U}^{*}_{\mathrm{l}} & \text{if } \lambda^{\mathrm{l}} \leqslant 0 < \lambda^{\mathrm{m}} \\ \tilde{U}^{*}_{\mathrm{r}} & \text{if } \lambda^{\mathrm{m}} \leqslant 0 < \lambda^{\mathrm{r}} \\ \tilde{U}^{\mathrm{r}} & \text{if } \lambda^{\mathrm{r}} < 0 \end{cases} \tag{56}$$

DOI: 10.1002/fld

The corresponding interface flux, necessary to discretize (48), is calculated as

$$F_{i+1/2}=\begin{cases} F^{\mathrm{l}} & \text{if } \lambda^{\mathrm{l}}>0 \\ F_{\mathrm{l}}^{*} & \text{if } \lambda^{\mathrm{l}}\leqslant 0<\lambda^{\mathrm{m}} \\ F_{\mathrm{r}}^{*} & \text{if } \lambda^{\mathrm{m}}\leqslant 0<\lambda^{\mathrm{r}} \\ F^{\mathrm{r}} & \text{if } \lambda^{\mathrm{r}}<0 \end{cases} \tag{57}$$

with the following relations to calculate F_{l}^{*} and F_{r}^{*}:

$$\begin{aligned} F_{\mathrm{l}}^{*} &= F^{\mathrm{l}}+\lambda^{\mathrm{l}}(\tilde{U}_{\mathrm{l}}^{*}-\tilde{U}^{\mathrm{l}}) \\ F_{\mathrm{r}}^{*} &= F^{\mathrm{r}}-\lambda^{\mathrm{r}}(\tilde{U}_{\mathrm{r}}^{*}-\tilde{U}^{\mathrm{r}}) \end{aligned} \tag{58}$$

Finally, to completely define the Hermite-HLLC scheme, we need to precise the wave speeds; according to [14], we select the following solution:

$$\begin{aligned} \lambda^{\mathrm{l}} &\equiv \min(u^{\mathrm{l}}-a^{\mathrm{l}}, \hat{u}-\hat{a}) \\ \lambda^{\mathrm{r}} &\equiv \max(u^{\mathrm{r}}+a^{\mathrm{r}}, \hat{u}+\hat{a}) \\ \lambda^{\mathrm{m}} &\equiv u^{\mathrm{m}} \end{aligned} \tag{59}$$

where $\hat{}$ represents the classical Roe's average and $a^2\equiv\gamma p/\rho$ is the speed of sound for a perfect gas.

In [14], it is demonstrated that this choice of acoustic wave speeds, yields a positively conservative scheme. Therefore, this conclusion remains true in our formulation, at least in what concerns the variable U. Concerning the variable V, the problem of positivity preservation is more dubious since the notion of physically realistic states becomes difficult to define and interpret for spatial derivatives.

Remark 1

Resolution of isolated contact discontinuities. Suppose that the left and right states, $\tilde{U}_{\mathrm{l}}$ and $\tilde{U}_{\mathrm{r}}$, are connected by a single contact discontinuity. Then, we can write:

$$\begin{aligned} u^{\mathrm{l}} &= u^{\mathrm{r}}\equiv u \\ p^{\mathrm{l}} &= p^{\mathrm{r}}\equiv p \\ p_x^{\mathrm{l}} &= p_x^{\mathrm{r}}\equiv p_x \\ (\rho u_x)^{\mathrm{l}} &= (\rho u_x)^{\mathrm{r}}\equiv \rho u_x \end{aligned} \tag{60}$$

Inserting those relations into (53b) and (53c), we obtain: $p^{\mathrm{m}}=p$, $\rho_{\mathrm{l}}^{*}=\rho^{\mathrm{l}}$, $\rho_{\mathrm{r}}^{*}=\rho^{\mathrm{r}}$.

Therefore, one can conclude that $U_{\mathrm{l}}^{*}=U^{\mathrm{l}}$ and $U_{\mathrm{r}}^{*}=U^{\mathrm{r}}$.

In addition, (55a) gives: $\rho_x|_{\mathrm{l,r}}^{*}=\rho_x|_{\mathrm{l,r}}$. Therefore, we also have: $V_{\mathrm{l,r}}^{*}=V^{\mathrm{l,r}}$.

Consequently, the general solution for such a case, reads as

$$\tilde{U}_{i+1/2}=\begin{cases} \tilde{U}^{\mathrm{l}} & x<ut \\ \tilde{U}^{\mathrm{r}} & x>ut \end{cases} \tag{61}$$

DOI: 10.1002/fld

This solution is precisely the exact solution for an isolated contact discontinuity defined by relation (60).

Remark 2

Resolution of isolated shock waves. At an isolated shock wave, the shock velocity, s, is given by the largest (or the smallest) eigenvalue of the Roe matrix [9]. For example, suppose that the shock propagates to the right, i.e. $\lambda^{\mathrm{r}} \equiv s$.

Then, the Rankine–Hugoniot conditions for U yield

$$\lambda^{\mathrm{r}} \equiv s = \frac{(\rho u)^{\mathrm{l}} - (\rho u)^{\mathrm{r}}}{\rho^{\mathrm{l}} - \rho^{\mathrm{r}}} = \frac{(\rho u^2 + p)^{\mathrm{l}} - (\rho u^2 + p)^{\mathrm{r}}}{(\rho u)^{\mathrm{l}} - (\rho u)^{\mathrm{r}}} \tag{62}$$

Introducing these relations into (53a), we get: $u^{\mathrm{m}} = u^{\mathrm{l}}$. Using this result into (53b) and (53c), we obtain: $\rho_{\mathrm{l}}^* = \rho^{\mathrm{l}} = \rho_{\mathrm{r}}^*$ and $p_{\mathrm{l}}^* = p^{\mathrm{l}} = p_{\mathrm{r}}^*$. Therefore, there is a single wave that connects U^{l} and U^{r}.

This wave is such that

$$U_{i+1/2} = \begin{cases} U^{\mathrm{l}}, & x < st \\ U^{\mathrm{r}}, & x > st \end{cases} \tag{63}$$

This is the exact solution for an isolated shock wave that propagates at the velocity, s.

Now, let us consider relations for the variable, V.

If there exists an isolated shock wave connecting V^{l} and V^{r}, we have, necessarily

$$s' = \frac{(\rho u)_x^{\mathrm{l}} - (\rho u)_x^{\mathrm{r}}}{\rho_x^{\mathrm{l}} - \rho_x^{\mathrm{r}}} = \frac{(\rho u^2 + p)_x^{\mathrm{l}} - (\rho u^2 + p)_x^{\mathrm{r}}}{(\rho u)_x^{\mathrm{l}} - (\rho u)_x^{\mathrm{r}}} \tag{64}$$

However, there are no reasons that $s' \equiv s$.

Consequently, introducing (64) into (55b), we get the following result:

$$(\rho u_x)^{\mathrm{m}} = (\rho u_x)^{\mathrm{l}} + \frac{\lambda^{\mathrm{r}} - s'}{\lambda^{\mathrm{l}} - \lambda^{\mathrm{r}}} \times A \tag{65a}$$

where we defined the quantity: $A \equiv (\rho u)_x^{\mathrm{l}} - (\rho u)_x^{\mathrm{r}} - u^{\mathrm{l}}(\rho_x^{\mathrm{l}} - \rho_x^{\mathrm{r}})$.

Using this result into (55a), we obtain:

$$\rho_x|_{\mathrm{l}}^* = \rho_x^{\mathrm{l}} - \frac{(\lambda^{\mathrm{r}} - s')}{(\lambda^{\mathrm{l}} - \lambda^{\mathrm{r}})(u^{\mathrm{l}} - \lambda^{\mathrm{l}})} \times A \tag{65b}$$

$$\rho_x|_{\mathrm{r}}^* = \frac{\rho_x^{\mathrm{r}}(s' - \lambda^{\mathrm{r}}) + \rho_x^{\mathrm{l}}(u^{\mathrm{l}} - s')}{u^{\mathrm{l}} - \lambda^{\mathrm{r}}} - \frac{(\lambda^{\mathrm{r}} - s')}{(\lambda^{\mathrm{l}} - \lambda^{\mathrm{r}})(u^{\mathrm{l}} - \lambda^{\mathrm{l}})} \times A \tag{65c}$$

Lastly, (55c) gives the following result:

$$p_x^{\mathrm{m}} \equiv p_x|_{\mathrm{r}}^* = p_x|_{\mathrm{l}}^* = p_x^{\mathrm{l}} + \frac{(\lambda^{\mathrm{r}} - s')(\lambda^{\mathrm{l}} - u^{\mathrm{l}})}{(\lambda^{\mathrm{l}} - \lambda^{\mathrm{r}})} \times A \tag{65d}$$

DOI: 10.1002/fld

Then, we can deduce the following statements:

- if $s' = \lambda^{\mathrm{r}}$, there is a single shock wave that connects V^{l} and V^{r}: this is the exact solution for V. This discontinuity propagates at the same velocity as the discontinuity in U.
- if $s' = u^{\mathrm{l}}$, then $A = 0$. Therefore, the single discontinuity that connects V^{l} and V^{r}, is a contact discontinuity, according to our definitions. This discontinuity does not coincide with the discontinuity in U. The consequence is that it can exist regions where U is continuous while V presents a discontinuity.
- In the general case, $s' \neq u^{\mathrm{l}}$ and $s' \neq \lambda^{\mathrm{r}}$. In that case, the discontinuity in V is not a contact discontinuity and does not propagate at the same velocity that the shock wave in U. We conclude that it may appear a Rankine–Hugoniot deficit in the solution for V. Indeed, the Rankine–Hugoniot conditions for the variable V, (64), give for example:

$$(\rho u)_x^{\mathrm{r}} - (\rho u)_x^{\mathrm{l}} = \lambda^{\mathrm{r}}(\rho_x^{\mathrm{r}} - \rho_x^{\mathrm{l}}) + (s' - \lambda^{\mathrm{r}})(\rho_x^{\mathrm{r}} - \rho_x^{\mathrm{l}}) \tag{66}$$

This relation means that, if we consider as solution a shock wave in (U,V), propagating at the velocity, λ^{r}, then, there necessarily exists a Rankine–Hugoniot deficit for the variable, V. According to (66), this deficit is quantified by the following quantity, for the variable ρ_x:

$$(s' - \lambda^{\mathrm{r}})(\rho_x^{\mathrm{r}} - \rho_x^{\mathrm{l}}) \tag{67}$$

As demonstrated in [11], this term is responsible for the existence of a singularity in the solution for V.

5. NUMERICAL VALIDATION

5.1. Spectral analysis

Our purpose is twofold: first we study the linear stability of the method, second we estimate the influence of the monotonicity parameter, α.

Technical details concerning this sub-section are given in Appendix A. To simplify the notations, we suppose that the mesh is uniform ($\Delta x_i = \Delta x \equiv \mathrm{Cte}$).

To study the spectral behaviour of the HLSM scheme, we consider the linear system that follows:

$$U_t + aU_x = 0 \quad (a \equiv \mathrm{Cte} > 0) \tag{68}$$

with: $U \equiv [u, r \equiv u_x]^{\mathrm{t}}$.

Using the so-called 'method of lines' and first discretizing the spatial operator, we obtain the following system of ODEs in time:

$$\left.\frac{\mathrm{d}U}{\mathrm{d}t}\right|_i + a\frac{U_{i+1/2}^{\mathrm{l}} - U_{i-1/2}^{\mathrm{l}}}{\Delta x} = 0 \tag{69}$$

Then, a discrete Fourier transform gives the following result, for the complex amplitude of the solution, $\hat{U}$ (see Appendix for a detailed explanation):

$$\frac{\mathrm{d}\hat{U}}{\mathrm{d}t} = G(\beta, \nu, \alpha) \times \hat{U} \tag{70}$$

DOI: 10.1002/fld

Finally, integrating this result by the third-order TVD Runge–Kutta scheme, (10), over the interval $[t_n, t_{n+1}]$, we obtain:

$$\hat{U}^{n+1} = \mathscr{G}(\beta, \nu, \alpha) \times \hat{U}^n \tag{71}$$

In the Fourier space, this relation is equivalent to the integrated form of (69) in the physical space. Therefore, to study the structure of the 2×2 complex matrix, Γ, is equivalent to analyse the space–time properties of the algebraic form discretizing (68).

This complex matrix, $\mathscr{G}(\beta, \nu, \alpha)$—also called in the literature, the 'complex amplification matrix'—makes it possible to define the following quantities (see Appendix A for details):

- the 'accurate' and 'spurious' eigenvalues,
- discretization and 'spurious' errors,
- the truncature error,
- the amplitude and phase errors.

All these quantities can be expressed in terms of the three parameters of this study: the number of cells-per-wavelength, N ($N \times \beta = 2\pi$), the CFL number, ν ($\equiv a\Delta t/\Delta x$) and the monotonicity parameter, α, introduced to modulate w_i, (Formula (33)).

To begin this analysis, we select the case $w_i = \alpha \times \Delta x^4$ in the algebraic relations defining the HLSM interpolation. In other words, we suppose that the numerical solution lies in a region of smoothness: in such a case, the choice of the monotonicity constraint is indifferent. Unless mentioned, the CFL number is set to 0.8 in these results. Figure 3 presents results for a centred initialization of the first derivative ($r(x_i, t=0) = (u(x_{i+1}, t=0) - u(x_{i-1}, t=0))/2\Delta x$).

As one can note, the modulus of both accurate and spurious eigenvalues remains everywhere below unity; the scheme is linearly stable, Figure 3(a). This is true as long as the CFL is lower than the unity; in the opposite case, the modulus of the accurate eigenvalue becomes greater than one and the scheme is unstable. Figure 3(b) shows a very interesting result: at a given time ($t = 100 \times \Delta t$) and whatever the spatial discretization selected (β varying), the 'spurious' error remains lower than the truncature and the discretization errors. To verify if this result is preserved in time, we present Figure 3(c): as we can note, the magnitude of the 'spurious' error on a given mesh—$N = 10$ cells-per-wavelength: a reasonable choice for a high-order scheme—decreases very rapidly when the time grows up. Therefore, we can conclude that the spurious component of the numerical solution never 'pollutes' the accurate component of that solution. Finally, Figure 3(d), checks the global accuracy of the method by plotting the truncature error versus the phase angle: the global third-order accuracy is confirmed.

Furthermore, we can analytically formulate in the Fourier space, the spatial truncature error, $\hat{\tau}(\beta)$, when $\beta \to 0$ (see Appendix A).

Indeed, by using a Taylor series expansion in β, the result is the following:

$$\hat{\tau} = \tfrac{1}{360}\beta^5 + O(\beta^6) \tag{72}$$

Obviously, this result indicates that the spatial accuracy of the scheme—fifth-order accuracy—is free of the value of the monotonicity parameter, α. This result is equivalent to formulae (39) obtained in the physical space. Therefore, we can conclude that α *has no influence on the accuracy of the solution in regions of smoothness*: α is only selected to optimize the capture of discontinuities.

Now, if we modify the initialization process of the first derivative, the result is somewhat different: this is illustrated by Figure 4. For an upwind first-order discretization, the level of the

DOI: 10.1002/fld

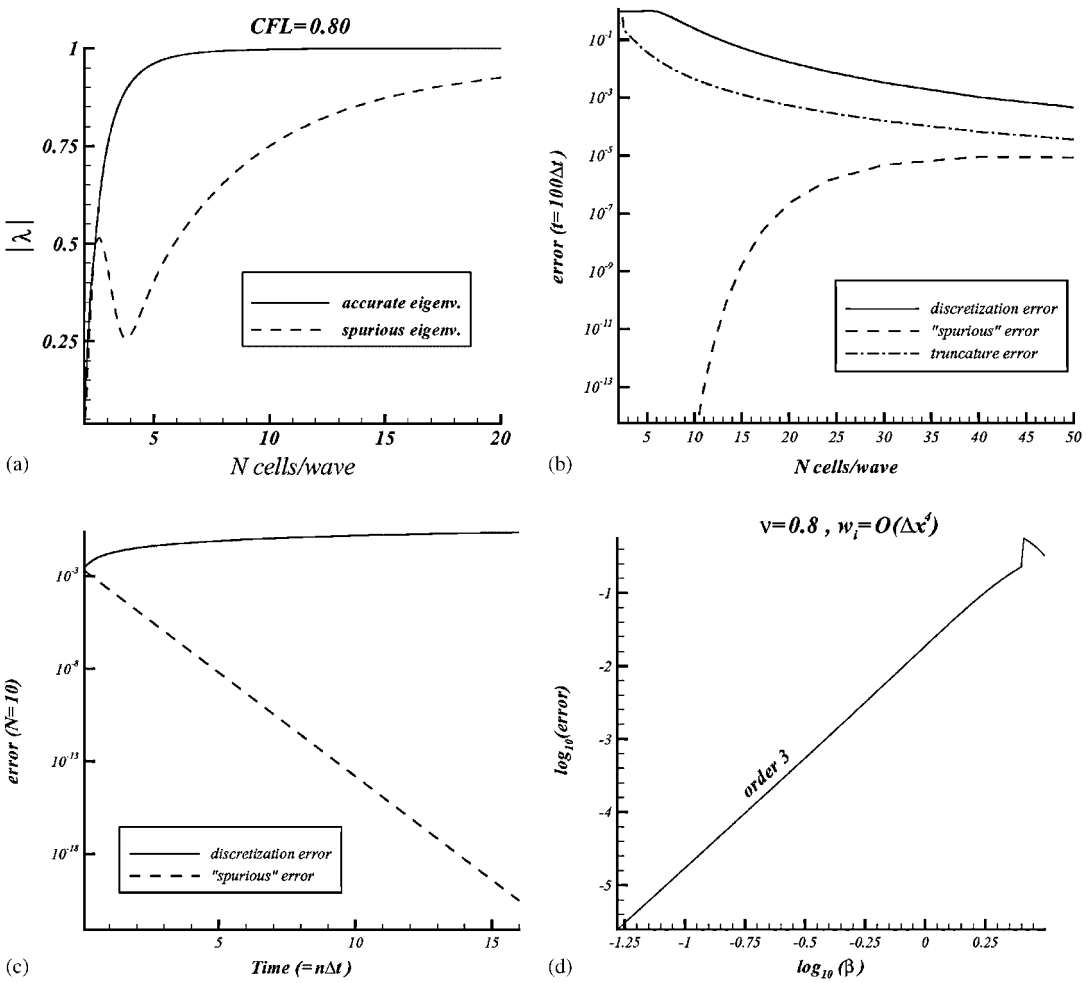

Figure 3. Spectral analysis for the HLSM scheme (centred initialization of the derivative): $v=0.80$, $w_i=\alpha\times\Delta x^4$: (a) accurate and spurious eigenvalues; (b) spatial evolution of errors at $t_n=100\times\Delta t$; (c) temporal evolution of errors for $N=10$ cells-per-wavelength; and (d) total truncature error.

initial error becomes higher: in some cases ($N\geqslant 35$) this increase can generate a 'spurious' error greater than the truncature error, Figure 4(a). However, even in this case, the 'spurious' error rapidly decreases when the time grows up, Figure 4(b). This tendency is unchanged when the first derivative is initialized to the zero value, Figure 4(c) and (d).

Lastly, Figure 5 presents the levels of the amplitude and phase errors according to N and the CFL.

As one can see, only 12 cells-per-wavelength are necessary to get an amplitude error at 0.1% for CFL$=0.8$. For this latter value, less than 10 cells-per-wavelength are necessary to get a 0.1% phase error.

Now, we look at the case $w_i=O(\alpha)$.

DOI: 10.1002/fld

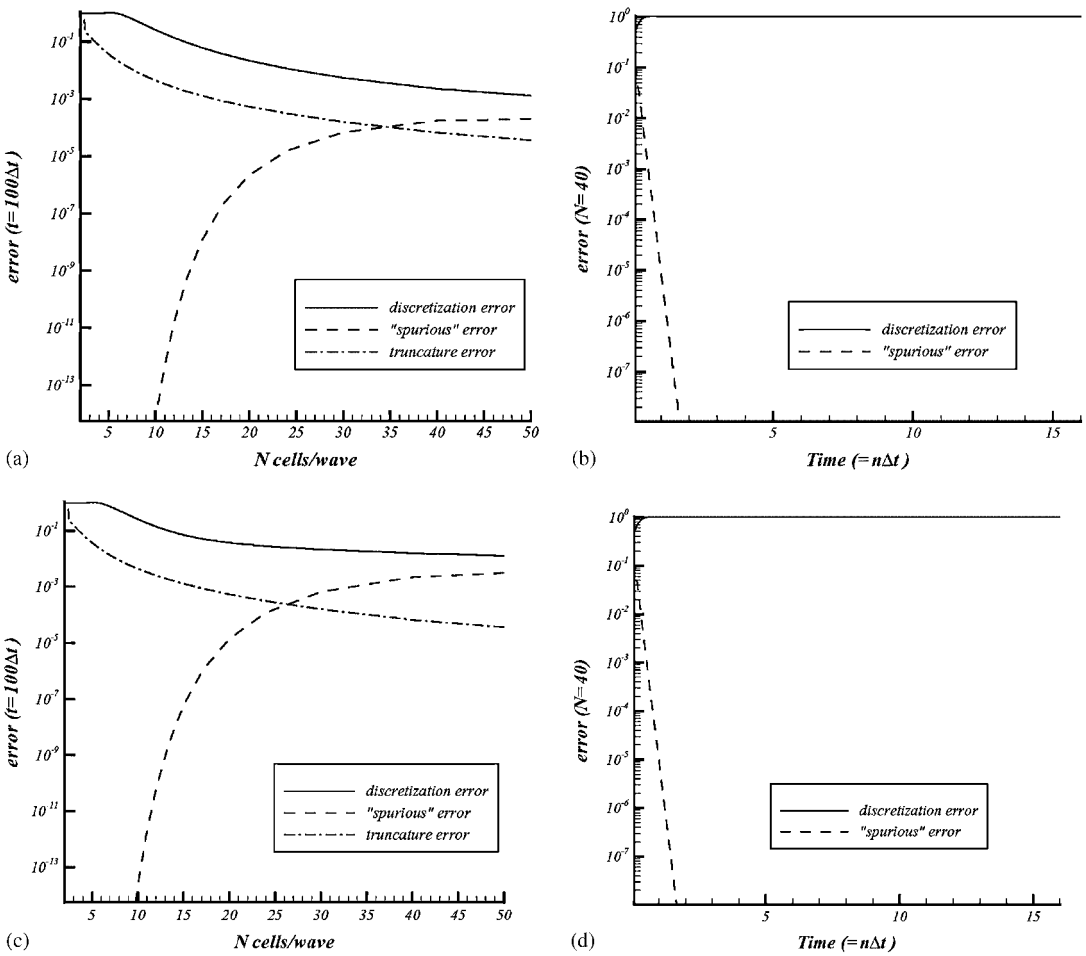

Figure 4. Spectral analysis for the HLSM scheme: $v=0.80$, $w_i=\alpha\times\Delta x^4$. Initialization of the first derivative (a), (b): $r(x_i,t=0)=u(x_i,t=0)-u(x_{i-1},t=0)/\Delta x$; (c), (d): $r(x_i,t=0)\equiv 0$; (a), (c): spatial evolution of errors at $t_n=100\times\Delta t$; (b), (d): temporal evolution of errors for $N=40$ cells-per-wavelength.

As already mentioned, this case can correspond to two cases for the TVD constraint, (36): (i) the presence of a discontinuity in the solution, (ii) the existence of an extremum.

In that case, the Minmod function returns the zero value for the local slope of the solution ($\tilde{B}_5=\tilde{B}_6=0$). Inserting this result into the complex amplification matrix, we obtain the following result concerning the spatial truncature error:

$$\hat{\tau}=\frac{\alpha^2}{2(\alpha^2+4)}\beta+O(\beta^2) \tag{73}$$

As predicted, the scheme becomes first order; moreover, the size of the truncature error now depends on the value of α: the dissipative nature of the scheme can be modulated by the value of α. This result means that the numerical handling of a discontinuity will be influenced by the

DOI: 10.1002/fld

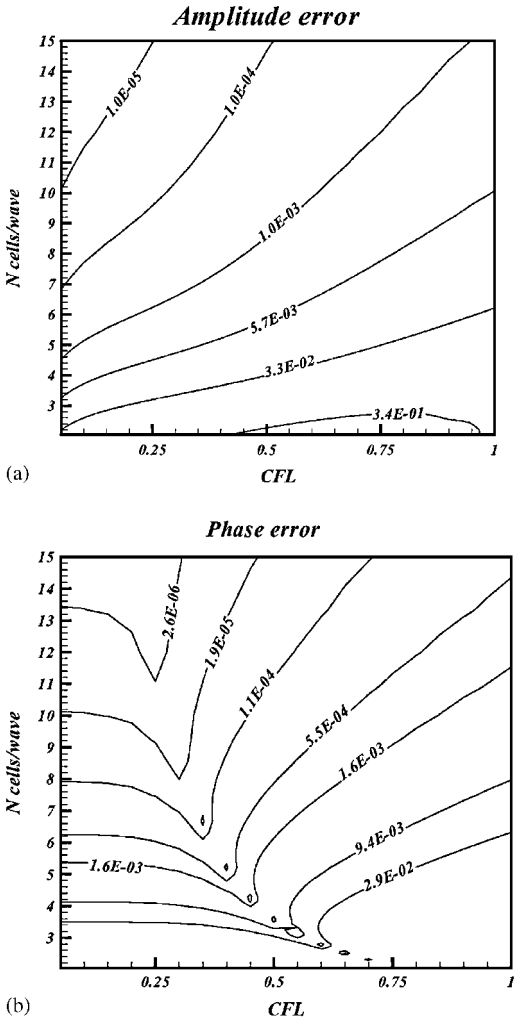

Figure 5. Spectral analysis for the HLSM scheme: $v=0.80$, $w_i=\alpha\times\Delta x^4$: (a) amplitude error and (b) phase error.

choice of the parameter, α, as already noted in the accuracy analysis. Figure 6(a) and (b) present numerical phase and amplitude errors for this case: comparing to Figure 5 the loss of accuracy is clearly visible.

Summarizing, this analysis gives us two significant results:

- The accuracy of the scheme is free of the monotonicity parameter, α. This parameter is only useful to optimize the capture of possible discontinuities.
- The initialization process of the first derivative has no influences upon the stability or the accuracy of the scheme as long as the CFL is lower than one.

DOI: 10.1002/fld

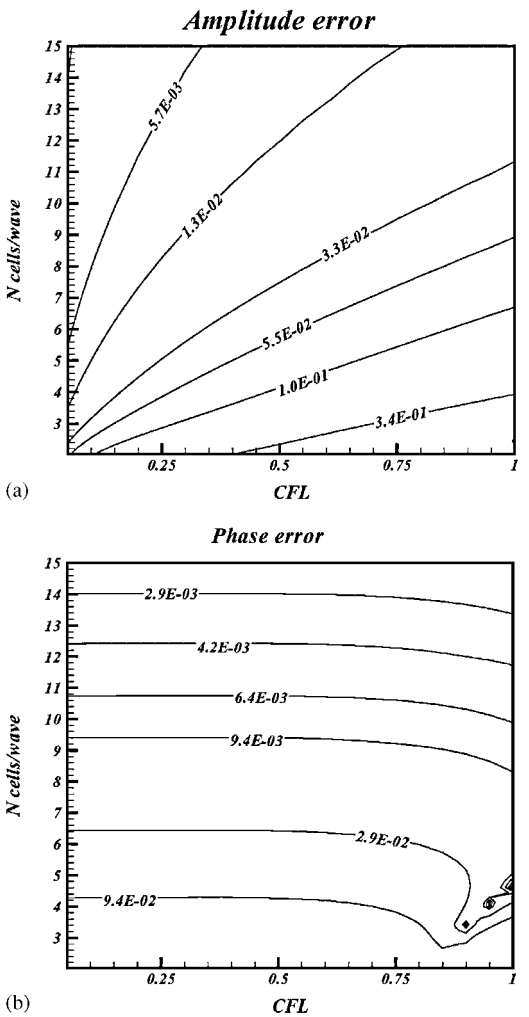

Figure 6. Spectral analysis for the HLSM scheme. Discontinuous case: $w_i = O(1)$: (a) amplitude error and (b) phase error.

For the entire scalar test cases that follow, the monotonicity parameter, α*, is set to the value* 6. This value was optimized by trial and errors when discontinuities are present in the solution.

5.2. Nonlinear scalar problem: the Burgers equation

We solve for the following nonlinear scalar Burgers equation:

$$u_t + \left(\frac{u^2}{2}\right)_x = 0 \quad \forall x \in [0, 2] \tag{74}$$

DOI: 10.1002/fld

Table I. Burgers equation: continuous case.

N	L_1 error	L_1 order	L_∞ error	L_∞ order	CPU_time
10	1.36×10^{-2}	—	2.56×10^{-2}	—	—
20	5.01×10^{-4}	4.8	2.32×10^{-3}	3.1	—
40	8.05×10^{-6}	5.9	4.18×10^{-5}	5.8	4×10^{-2}
80	2.52×10^{-7}	5	1.95×10^{-6}	5	0.30
160	8.27×10^{-9}	5	6.35×10^{-8}	5	2.46

$u_t+uu_x=0$; $u(x,t=0)=\frac{1}{2}+\sin(\pi\times x)$; HLSM-Minmod scheme ($\alpha=6$) with periodic boundary conditions; $t=\frac{1}{2}\pi$; $\Delta t=\Delta x^2/2$; L_1 and L_∞ errors for $u(x)$.

Table II. Burgers equation: continuous case.

N	L_1 error	L_1 order	L_∞ error	L_∞ order
10	5.0×10^{-2}	—	0.12	—
20	2.28×10^{-2}	2.1	1.85×10^{-1}	0.6
40	2.56×10^{-3}	3.2	2.61×10^{-2}	2.8
80	1.76×10^{-4}	3.8	2.54×10^{-3}	3.1
160	1.17×10^{-5}	4	1.72×10^{-4}	3.9
320	7.32×10^{-7}	4	1.12×10^{-5}	4

$u_t+uu_x=0$; $u(x,t=0)=\frac{1}{2}+\sin(\pi\times x)$; HLSM-Minmod scheme ($\alpha=6$) with periodic boundary conditions; $t=\frac{1}{2}\pi$; $\Delta t=\Delta x^2/2$; L_1 and L_∞ errors for $u_x(x)$.

Table III. Burgers equation: continuous case.

N	L_1 error	L_1 order	L_∞ error	L_∞ order
20	9.13×10^{-3}	—	4.63×10^{-2}	—
40	4.21×10^{-4}	4.4	2.26×10^{-3}	4.1
80	7.42×10^{-6}	5.8	6.72×10^{-5}	5
160	5.40×10^{-7}	5.3	1.75×10^{-6}	5.2

$u_t+uu_x=0$; $u(x,t=0)=\frac{1}{2}+\sin(\pi\times x)$; HLSM-Minmod scheme ($\alpha=6$) with periodic. boundary conditions; $t=\frac{1}{2}\pi$; $\Delta t=\Delta x_{\min}^2/2$; L_1 and L_∞ errors for $u(x)$. Non-uniform meshes ($\Delta x_{\max}/\Delta x_{\min}\approx4, N=160$).

with the initial condition: $u(x,t=0)=\frac{1}{2}+\sin(\pi x)$ and a two-periodic boundary condition. A uniform mesh with N cells is used in Tables I, II and IV, while Table III is obtained by generating non-uniform meshes. The non-uniform meshes are generated such that the stretching is intense in the central zone of the domain where the solution is highly varying. In addition, we utilize the HUWENO5 scheme of Qiu and Shu [15], as a reference for the accuracy tests and CPU time efforts. The CFL number is defined as: $\max_i|u_i^n|\Delta t/\min_i\Delta x_i$; unless mentioned, its value is taken as 0.5 for both HLSM and HUWENO5 schemes. For the accuracy tests, since the time-integration method incurs $O(\Delta t^3)$ errors, the time step is chosen to be $\Delta t=O(\Delta x^2)$ in order for the discretization error of the overall scheme to be a measure of the spatial convergence only.

DOI: 10.1002/fld

Table IV. Burgers equation: continuous case.

N	L_1 error	L_1 order	L_∞ error	L_∞ order	CPU_time
10	3.66×10^{-3}	—	7.29×10^{-3}	—	—
20	1.86×10^{-4}	4.1	8.03×10^{-4}	3	—
40	1.07×10^{-5}	3.9	6.06×10^{-5}	3.5	1×10^{-2}
80	3.54×10^{-7}	4.9	2.73×10^{-6}	4.5	7×10^{-2}
160	1.20×10^{-8}	4.9	9.27×10^{-8}	4.9	0.60

$u_t+uu_x=0$; $u(x,t=0)=\frac{1}{2}+\sin(\pi\times x)$; HUWENO5 scheme with periodic boundary conditions; $t=\frac{1}{2}\pi$; $\Delta t=\Delta x^2/2$; L_1 and L_∞ errors.

When $t=\frac{1}{2}\pi$, the solution is still smooth and the discrete errors (L_1 and L_∞ norms) and numerical orders of accuracy are shown in Table I (HLSM-Minmod scheme, $u(x)$ profile), Table II ($u_x(x)$ profile), Table III (HLSM-Minmod scheme on non-uniform meshes, $\Delta x_{\max}/\Delta x_{\min}\approx4$, for $N=160$ grid points) and Table IV (HUWENO5 scheme). As can be seen, both schemes reach their theoretical order of accuracy and give equivalent results on uniform meshes. On non-uniform meshes, the error level of the HLSM scheme increases but its high-order accuracy is maintained. As one can note it, the HLSM scheme (Table I) is much more costly than a more classical WENO procedure (Table IV). The reason is twofold: first, the least-square reconstruction is devised to be used on irregular meshes and it is thus algebraically more complicated; second, the monotonicity constraints introduced into the least-square system force to invert this one, at each time step.

When $t=\frac{3}{2}\pi$, a shock has already appeared in the solution and it is located at $x=1.238$.

Figure 7 shows the numerical solution for the HLSM scheme on a uniform mesh with $N=80$ grid points. As one can note in Figure 7(a), the shock is captured without any numerical oscillation in all cases. Figure 7(b) shows the evolution of w_i in the computation domain: only four values are $O(1)$. It is at these points that the monotonicity constraints play a role. Figure 8(a) shows the numerical solution on a stretched mesh ($\Delta x_{\min}/\Delta x_{\max}=0.10$) near the shock place: the shock is captured without any numerical oscillations. Lastly, Figure 8(b) gives a comparison with results obtained with the HUWENO5 scheme, on a uniform mesh ($N=80$): whatever the numerical method selected, the shock is captured in the same way.

Consequently, the monotonicity constraints (21), produce numerical results that are equivalent to those obtained via a more classical WENO procedure. Those results are largely preserved on non-uniform meshes; however, the increased algebraic complexity of the resulting scheme results in an increased computational time.

5.3. Non-convex fluxes

We use two non-convex fluxes to study the convergence of the scheme to the physically correct solution. The 'exact' solutions are obtained from the HLSM scheme on a very fine grid. All the results presented below are obtained with $N=80$ grid points.

The first example is a Riemann problem with the flux selected as

$$f(u)=\tfrac{1}{4}(u^2-1)(u^2-4) \tag{75}$$

DOI: 10.1002/fld

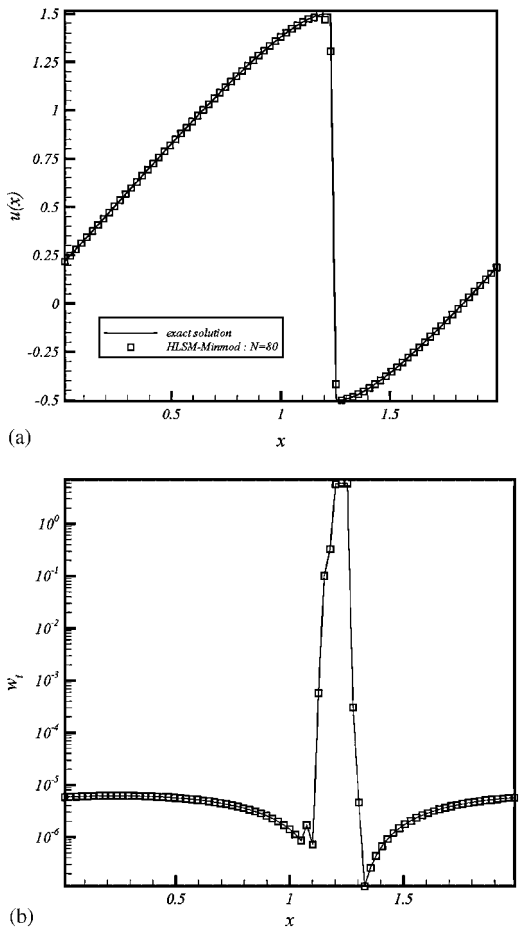

Figure 7. Burgers equation. $u(x,t=0)=\frac{1}{2}+\sin(\pi x)$, $t=\frac{3}{2}\pi$, $N=80$, CFL$=0.5$, $\alpha=6$. HLSM scheme: (a) HLSM-Minmod and (b) data-depending weight, w_i.

with the initial data

$$u(x,t=0)=\begin{cases} u_\mathrm{l} & x<0 \\ u_\mathrm{r} & x>0 \end{cases}$$

The first case we test is: $u_\mathrm{l}=2, u_\mathrm{r}=-2$, Figure 9. The exact solution is a centred rarefaction wave between two discontinuities. Numerical results are presented at $t=1.20$. As one can see, the HLSM scheme gives the entropy correct solution, with no significant oscillations at discontinuities.

The second case is: $u_\mathrm{l}=-3, u_\mathrm{r}=3$, Figure 10. The exact solution is a stationary shock at $x=0$ with two rarefaction waves. Numerical results are presented at $t=0.05$. To get those results, we had to lower the CFL number to the value 0.05. Once again, the HLSM scheme gives the correct solution; we observe that the stationary shock is correctly resolved.

DOI: 10.1002/fld

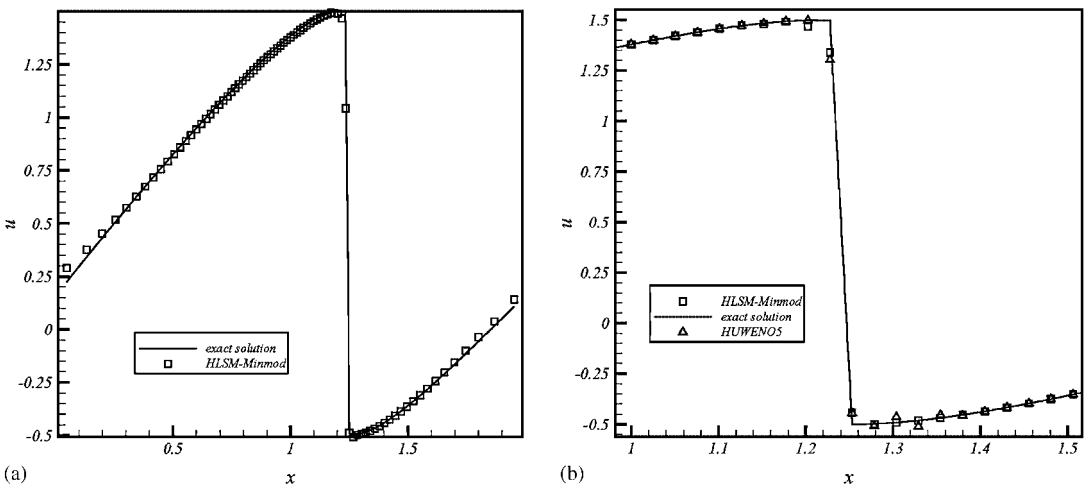

Figure 8. Burgers equation. $u(x,t=0)=\frac{1}{2}+\sin(\pi x)$, $t=\frac{3}{2}\pi$, $N=80$, CFL$=0.5, \alpha=6$: (a) HLSM-Minmod: non-uniform mesh ($\Delta x_{\min}/\Delta x_{\max}=0.1$) and (b) comparison between the HLSM-Minmod scheme and the HUWENO5 scheme.

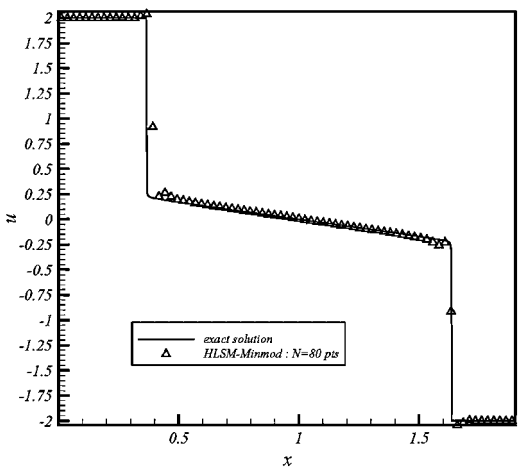

Figure 9. HLSM-Minmod. Non-convex flux: $f(u)=\frac{1}{4}(u^2-1)(u^2-4)$, $u_l=2$, $u_r=-2$. $t=1.20$, $N=80$, CFL$=0.5$, $\alpha=6$.

The second flux is the Buckley–Leverett flux:

$$f(u)=\frac{4u^2}{(4u^2+(1-u)^2)} \tag{76}$$

DOI: 10.1002/fld

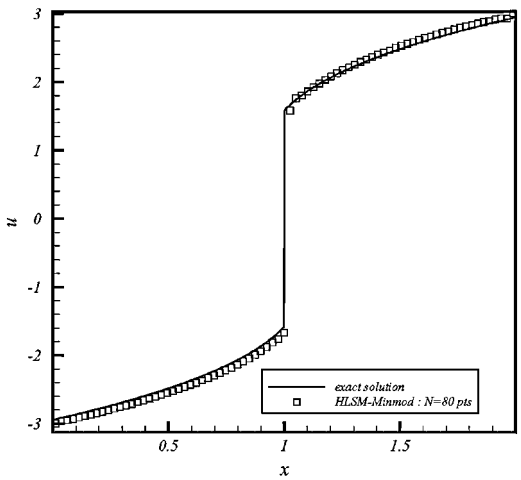

Figure 10. HLSM-Minmod. Non-convex flux: $f(u)=\frac{1}{4}(u^2-1)(u^2-4)$, $u_l=-3$, $u_r=3$. $t=5\times10^{-2}$, $N=80$, CFL$=0.05$, $\alpha=6$.

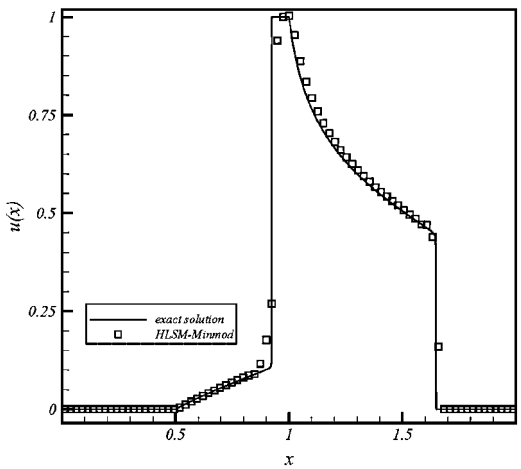

Figure 11. HLSM-Minmod. Buckley–Leverett flux. $t=0.40$, $N=80$, CFL$=0.5$, $\alpha=6$.

with initial data

$$u=\begin{cases}1 & \forall x\in[-1/2,0]\\ 0 & \text{otherwise}\end{cases}$$

The exact solution is a shock-rarefaction-contact discontinuity mixture. The solution is computed up to $t=0.40$. The result is displayed in Figure 11. The numerical solution is in good agreement with the entropy solution.

DOI: 10.1002/fld

5.4. 1D hyperbolic systems: the Euler equations

In order to extend the HLSM procedure defined in the scalar case, the conservative point values $(U^{l,r}_{i+1/2}, V^{l,r}_{i+1/2})$ are calculated from the interpolated primitive variables $[\rho^{l,r}_{i+1/2}, u^{l,r}_{i+1/2}, p^{l,r}_{i+1/2}]^t$ and $[(\rho_x)^{l,r}_{i+1/2}, (u_x)^{l,r}_{i+1/2}, (p_x)^{l,r}_{i+1/2}]^t$. Those variables are interpolated by using the HLSM procedure developed in the scalar case. Although the choice of primitive variables is not referenced in the literature as the best one for dealing with 1D problems (a characteristic-wise reconstruction would be more suitable [16]) it has the advantage of being general since its extension to multi-dimensional problems is straightforward.

Unless mentioned, all the test cases that follow are run with $\alpha=2.5$. This value is selected as the best compromise for the cases investigated.

The computations are run on a uniform mesh ($\Delta x_i \equiv \text{Cte}$), except for the last test case (the transonic nozzle). N grid points are utilized to discretize the equations.

The CFL number is defined as

$$\text{CFL} \equiv \Delta t \times \frac{\max_i(|u_i|+a_i)}{\Delta x}$$

We choose CFL$=0.50$ for almost all test cases, except for the accuracy tests.

Example 1

Accuracy tests: smooth solution. We solve the extended Euler equations (48), into the domain $[0, 2]$. The initial condition is set to be: $\rho(x, t=0)=1+0.2\times\sin(\pi x)$, $u(x, t=0)=1$, $p(x, t=0)=1$, with a two-periodic boundary condition. The numerical solution is computed up to $t=2$, with $\Delta t = O(\Delta x^2)$. The errors and numerical orders of accuracy for the density, ρ, and its first derivative, ρ_x, obtained with the Hermite-HLLC scheme, are shown in Tables V and VI. As one can note, the scheme reaches its theoretical order of accuracy both for the variable and its derivative. To compare with a WENO procedure, Table VII produces numerical results obtained with the HUWENO5 scheme [15]: the results are equivalent in terms of accuracy but the HLSM scheme is much more costly in terms of computational effort.

Example 2

Steady contact discontinuity [13]. We solve the extended Euler equations (48), with the initial data:

$$(\rho, u, p)^l = (1.4, 0, 1) \quad \forall x \leqslant 0.5, \quad (\rho, u, p)^r = (1, 0, 1) \quad \forall x > 0.5$$

Table V. 1D Euler equations $\rho(x, t=0)=1+0.2\times\sin(\pi x)$, $u(x, t=0)=1$, $p(x, t=0)=1$ Hermite-HLLC ($\alpha=2.5$) scheme with periodic boundary conditions.

N	L_1 error	L_1 order	L_∞ error	L_∞ order	CPU_time
10	4.42×10^{-3}	—	3.45×10^{-3}	—	1×10^{-2}
20	1.04×10^{-4}	5.4	8.13×10^{-5}	5.3	0.16
40	2.70×10^{-6}	5.2	2.12×10^{-6}	5.2	1.34
80	7.55×10^{-8}	5.2	5.93×10^{-8}	5.1	11.15
160	2.23×10^{-9}	5.1	1.88×10^{-9}	5	61

$t=2$; $\Delta t=\Delta x^2/2$; L_1 and L_∞ errors of density ρ.

DOI: 10.1002/fld

Table VI. 1D Euler equations $\rho_x(x,t=0)=0.2\times\pi\times\cos(\pi x)$, $u_x(x,t=0)=0$, $p_x(x,t=0)=0$ Hermite-HLLC scheme with periodic boundary conditions.

N	L_1 error	L_1 order	L_∞ error	L_∞ order
10	1.48×10^{-2}	—	1.16×10^{-2}	—
20	1.06×10^{-3}	3.8	8.34×10^{-4}	3.8
40	8.87×10^{-5}	3.6	6.96×10^{-5}	3.6
80	6.59×10^{-6}	3.8	5.18×10^{-6}	3.8
160	4.52×10^{-7}	3.9	3.55×10^{-7}	3.8

$t=2$; $\Delta t=\Delta x^2/2$; L_1 and L_∞ errors of density ρ_x.

Table VII. 1D Euler equations $\rho(x,t=0)=1+0.2\times\sin(\pi x)$, $u(x,t=0)=1$, $p(x,t=0)=1$ HUWENO5 scheme with periodic boundary conditions.

N	L_1 error	L_1 order	L_∞ error	L_∞ order	CPU_time
10	5.44×10^{-3}	—	4.25×10^{-3}	—	—
20	1.33×10^{-4}	5	1.04×10^{-4}	5	1×10^{-2}
40	3.64×10^{-6}	4.9	2.86×10^{-6}	4.9	0.10
80	1.06×10^{-7}	5.1	8.36×10^{-8}	5.1	0.59
160	3.22×10^{-9}	4.9	2.66×10^{-9}	4.8	3.85

$t=2$; $\Delta t=\Delta x^2/2$; L_1 and L_∞ errors of density ρ.

We use $N=100$ grid points and compute the solution until a final time $t=2$. Results are depicted in Figure 12. It is gratifying to note that the Hermite-HLLC scheme yields a clean jump in ρ, Figure 12(a). Figure 12(b) shows numerical results obtained with the Hermite-HLLE scheme: clearly, the introduction of the contact discontinuity into the Riemann solver has a strong impact.

Example 3
Moving contact discontinuity [13]. The initial data are now

$$(\rho,u,p)^{\mathrm{l}}=(1.4,0.1,1)\quad\forall x\leqslant 0.5,\qquad(\rho,u,p)^{\mathrm{r}}=(1,0.1,1)\quad\forall x>0.5$$

The numerical solution is computed for $N=100$ grid points at time $t=2$. Numerical results are displayed by Figure 13. Now, the results are smeared by the numerical viscosity introduced by the reconstruction scheme. However, the Hermite-HLLC solution, Figure 13(a), is less dissipative than the Hermite-HLLE version of the scheme, Figure 13(b). Therefore, the dissipative nature of the method is not only the consequence of the monotonicity constraints introduced into the reconstruction, but are also due to the choice of the approximate Riemann solver.

Example 4
Toro's Riemann problem [13]. Initial data are

$$(\rho,u,p)^{\mathrm{l}}=(1.,-19.59745,1000.)\quad\forall x\leqslant 0.8,\qquad(\rho,u,p)^{\mathrm{r}}=(1.0,-19.59745,0.01)\quad\forall x>0.8$$

The numerical solution is computed for $N=100$ grid points at time $t=0.012$.

DOI: 10.1002/fld

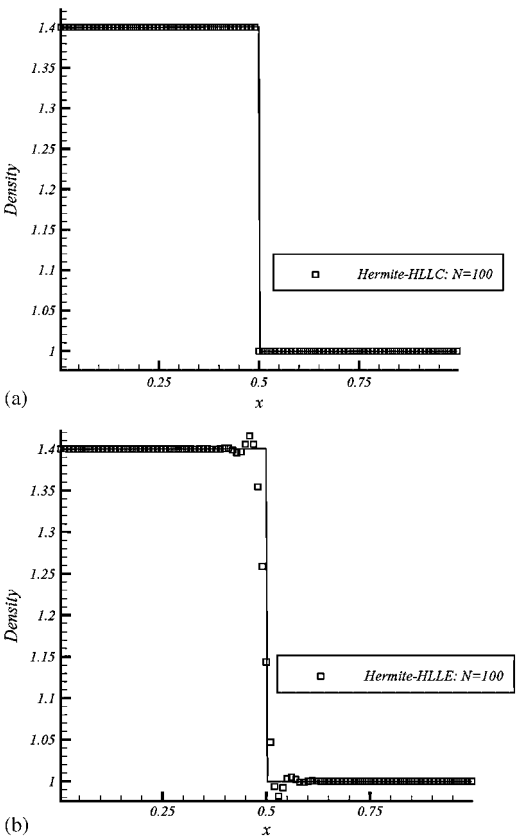

Figure 12. 1D Euler equations. Riemann problem: stationary contact discontinuity. $(\rho, u, p)^{\mathrm{l}} = (1.4, 0, 1)$ if $x < 0.5$; $(\rho, u, p)^{\mathrm{r}} = (1, 0, 1)$ if $x > 0.5$, $N = 100$, $t = 2$, CFL $= 0.5$: (a) Hermite-HLLC scheme and (b) Hermite-HLLE scheme.

The solution of this problem consists of a rarefaction wave travelling to the left, a stationary contact discontinuity and a shock wave travelling to the right. Numerical results are depicted in Figure 14.

Figure 14(a) presents the density profile obtained with the Hermite-HLLC scheme while Figure 14(b) displays the result obtained with the Hermite-HLLE scheme.

Once again, the contact discontinuity is correctly captured by the HLLC version of the scheme, Figure 14(a). If one uses the Hermite-HLLE scheme, instead, this discontinuity is more dissipated, as demonstrated by Figure 14(b).

When the mesh is refined, both schemes converge to the same solution.

Example 5

Toro's Riemann problem [13]. Initial data are

$$(\rho, u, p)^{\mathrm{l}} = (1., -2, 0.4) \quad \forall x \leqslant 0.5, \quad (\rho, u, p)^{\mathrm{r}} = (1., 2, 0.4) \quad \forall x > 0.5$$

DOI: 10.1002/fld

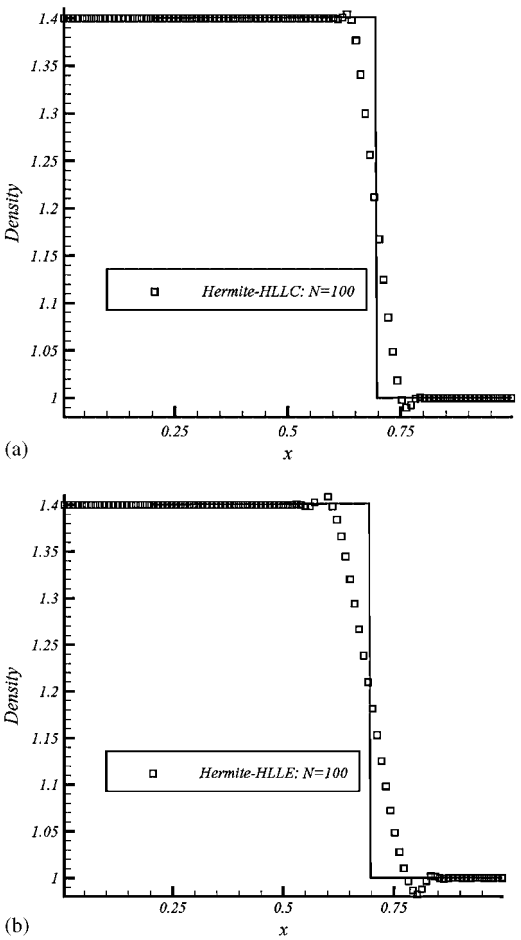

Figure 13. 1D Euler equations. Riemann problem: moving contact discontinuity. $(\rho, u, p)^{\mathrm{l}} = (1.4, 0.1, 1)$ if $x < 0.5$; $(\rho, u, p)^{\mathrm{r}} = (1, 0.1, 1)$ if $x > 0.5$, $N = 100$, $t = 2$, CFL $= 0.5$: (a) Hermite-HLLC scheme and (b) Hermite-HLLE scheme.

The numerical solution is computed for $N = 100$ grid points at time $t = 0.15$. Numerical results are displayed by Figure 15. The solution of this test consists of two symmetric rarefaction waves and a contact wave. The intermediate region between the rarefaction waves is close to vacuum. As one can note it, this region is correctly computed by the Hermite-HLLC scheme, Figure 15—left. The same conclusion is true for the Hermite-HLLE scheme except for the velocity profile that is slightly attenuated in the vacuum region, Figure 15—right.

In regions of smooth solution, one can note the high-order accuracy of the method that is especially visible in the distortion of the pressure and density profiles. When the mesh is refined, this distortion rapidly disappears.

In what follows, both schemes (Hermite-HLLE and Hermite-HLLC) share a similar behaviour: for this reason, we only show numerical results concerning the HLLC version.

DOI: 10.1002/fld

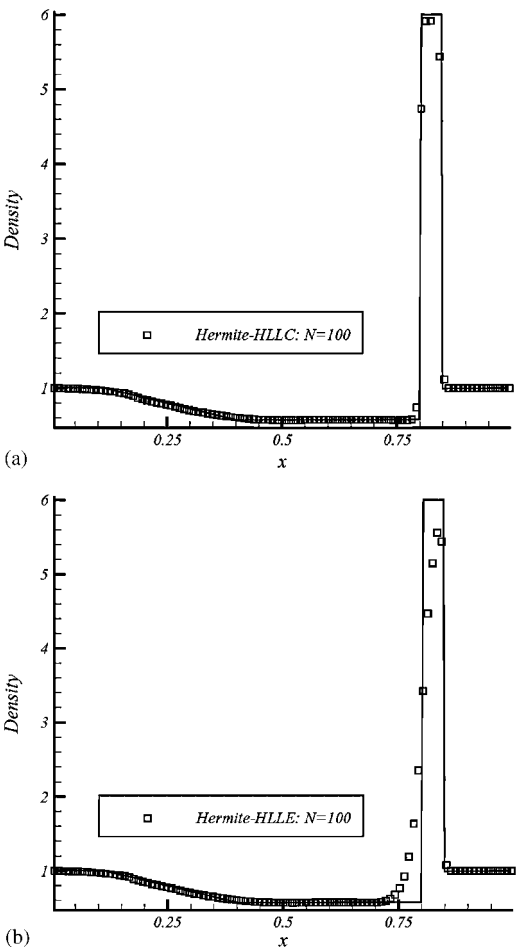

Figure 14. 1D Euler equations. Riemann problem. $(\rho, u, p)^{\mathrm{l}} = (1, -19.59745, 1000)$ if $x < 0.8$; $(\rho, u, p)^{\mathrm{r}} = (1, -19.59745, 0.01)$ if $x > 0.8$, $t = 0.012$, CFL $= 0.5$, $N = 100$: (a) Hermite-HLLC scheme and (b) Hermite-HLLE scheme.

Example 6

Sod's problem. The Sod problem is defined by the following left- and right-initial states:

$$(\rho, u, p)^{\mathrm{l}} = (1., 0.75, 1.) \quad \forall x \leqslant 0.3, \quad (\rho, u, p)^{\mathrm{r}} = (0.125, 0, 0.1) \quad \forall x > 0.3$$

$N = 100$ grid points are used to discretize the computational domain. The solution is run up to $t = 0.20$. We can see that the Hermite-HLLC scheme performs reasonably well, Figure 16. The shock wave is almost free of numerical oscillations and the contact discontinuity is not too much smeared.

Example 7

Shock interaction with entropy waves: *the Shu–Osher problem* [12]. We solve the extended Euler equations (48), with a moving Mach $= 3$ shock interacting with sine waves in density.

DOI: 10.1002/fld

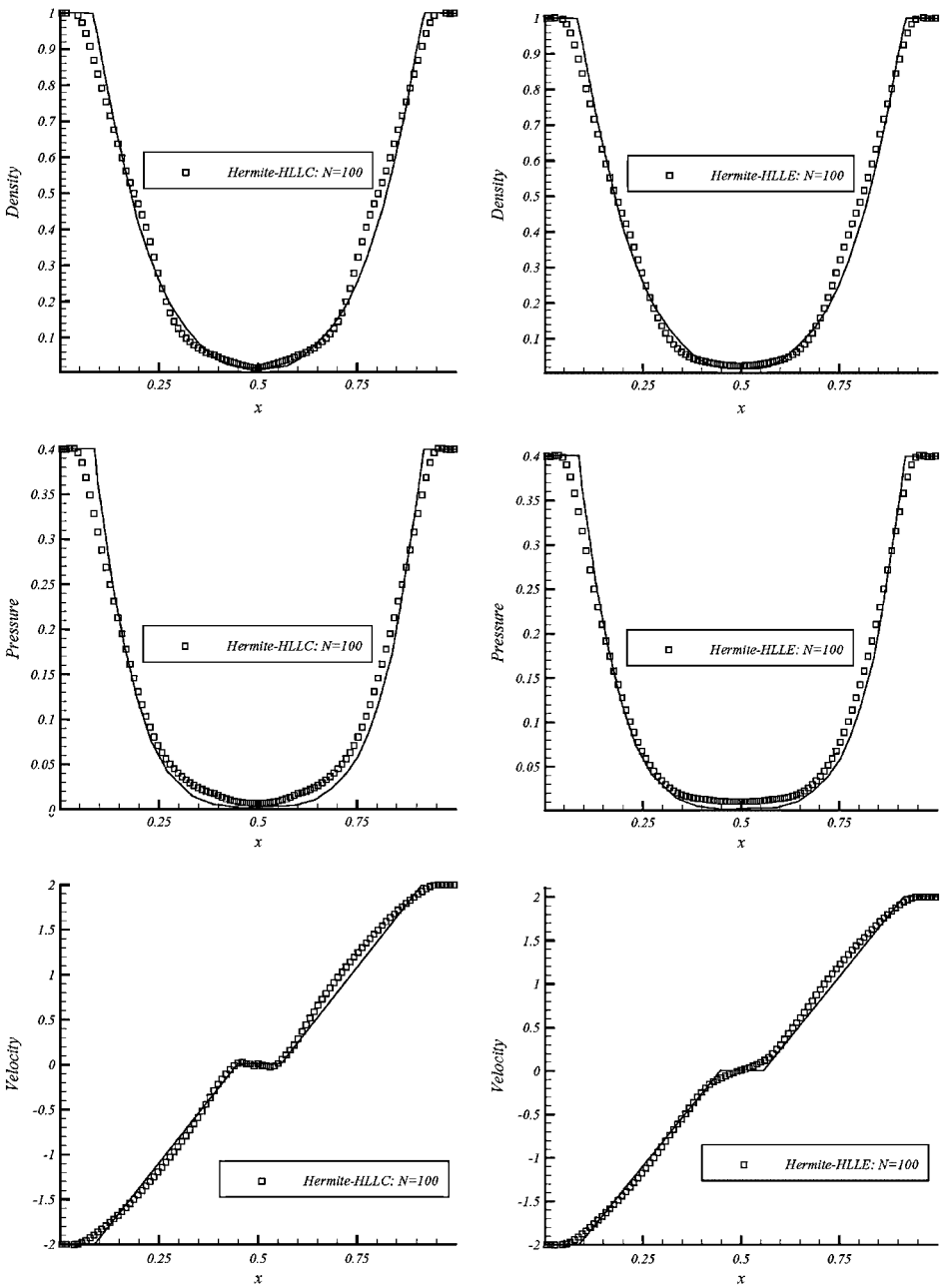

Figure 15. 1D Euler equations. Riemann problem. $(\rho, u, p)^{\mathrm{l}} = (1, -2, 0.4)$ if $x < 0.5$; $(\rho, u, p)^{\mathrm{r}} = (1, 2, 0.4)$ if $x > 0.5$, $N = 100$, $t = 0.15$, CFL $= 0.5$. Left: Hermite-HLLC scheme. Right: Hermite-HLLE scheme.

DOI: 10.1002/fld

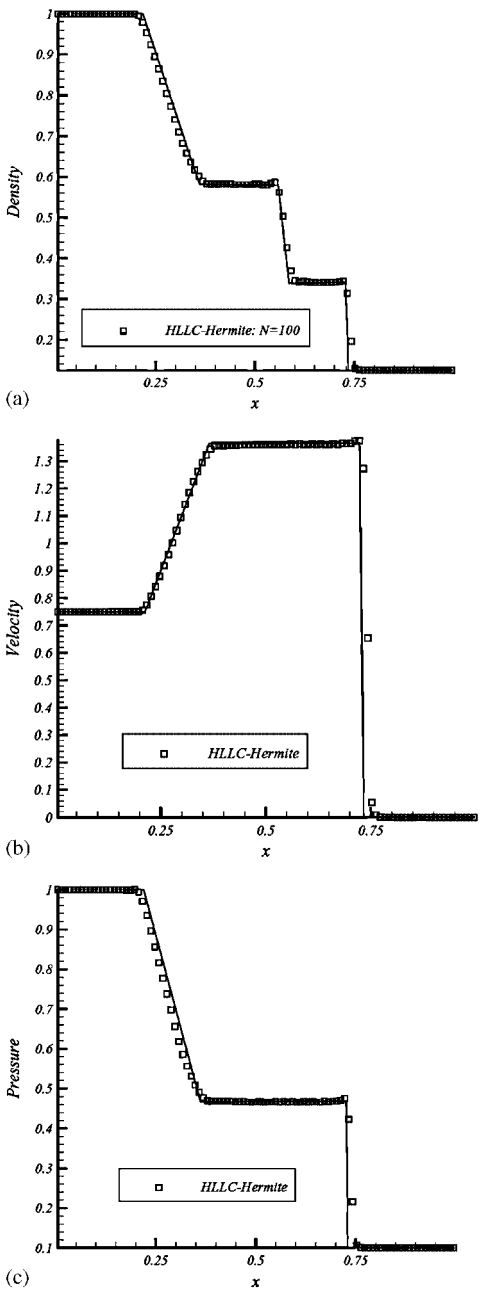

Figure 16. The Sod problem. Hermite-HLLC scheme. $N = 100$, $t = 0.20$, CFL $= 0.5$: (a) density; (b) velocity; and (c) pressure.

DOI: 10.1002/fld

The initial condition is defined as

$$(\rho, u, p) = (3.857143, 2.629369, 10.333333) \quad \forall x < -4$$

$$(\rho, u, p) = (1 + \delta \sin 5x, 0, 1) \quad \forall x \geqslant -4$$

For this test, we take $\delta = 10^{-2}$. The computed density ρ is plotted at $t = 1.8$ against the 'exact' solution; this solution is a converged solution computed by the HLLC scheme with 2500 grid points. Numerical results are displayed by Figure 17.

For $N = 300$ grid points, the shock entropy wave interaction is still underestimated. For $N = 400$ the interaction pattern is correctly predicted.

Example 8

Shock entropy wave interactions [4]. This problem is very suitable for high-order shock-capturing

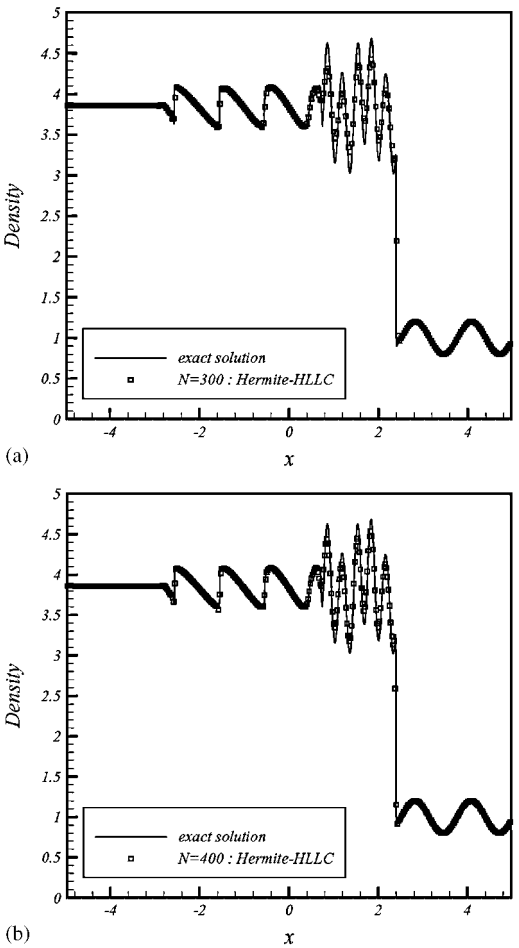

Figure 17. Shu–Osher problem. Hermite-HLLC scheme. $t = 1.80$, CFL = 0.5: (a) $N = 300$ and (b) $N = 400$.

DOI: 10.1002/fld

schemes because both shocks and complicate smooth flow features co-exist. In this example, a moving shock interacts with an entropy wave of small amplitude.

On the domain [0, 5], the initial condition is the following:

$$(\rho, u, p) = (3.857143, 2.629369, 10.333333) \quad \forall x < 1/2$$

$$(\rho, u, p) = (\mathrm{e}^{-\varepsilon \sin(kx)}, 0, 1) \quad \forall x \geqslant 1/2$$

where ε and k are the amplitude and the wave number of the entropy wave, respectively.

The mean flow is a right moving Mach 3 shock. If ε is small compared with the shock strength, the shock will go to the right of the computational domain, at approximately the non-perturbed shock speed and generate a sound wave that travels along with the flow behind the shock. At the same time, the small amplitude, low-frequency entropy waves are generated in front of the shock. After having interacted with the shock, these waves are compressed in frequency and amplified in amplitude.

The main goal of such a test is to check if the structure of the amplified waves is not lost after having crossed the shock wave. Since the entropy wave is very weak relative to the shock, any excessive numerical oscillation or dissipation could alter the generated waves and the entropy waves.

In our computations, we take $\varepsilon = 0.01$. Accordingly, the amplitude of the amplified entropy waves predicted by a linear analysis [17, 18], is 0.08690716 (shown in the following figures as horizontal solid lines). The pre-shock wave number, k, is selected such that $k = 13$. In order to get rid of the transient waves due to the initialization, the numerical procedure is defined so that the shock crosses the computational domain twice. The numerical solution is examined when the shock reaches $x = 4.5$ for the second time. For those computations, the CFL is lowered to the value 0.250. The numerical results are shown in Figure 18, for the entropy wave.

To begin, we use 400 grid points that is effectively 10 points in each wavelength of the generated entropy wave. We can see that the Hermite-HLLC scheme calculates the amplified entropy waves quite well, although their amplitude is still attenuated, Figure 18(a). On a grid of 800 points, Figure 18(b), the resolution becomes good.

Example 9

Propagation of sound waves through a transonic nozzle [19]. The computation of sound propagating through a choked nozzle presents a challenging problem for a shock-capturing scheme. To reduce the complexity of the problem, but retaining the basic physics and difficulties, this propagation problem is modelled by a 1D acoustic wave transmission problem through a transonic nozzle [19].

In this problem, an acoustic wave is introduced at the nozzle inflow region and the sound wave that travels downstream through the transonic nozzle and interacts with the shock is to be calculated. The amplitude of the incoming sound wave is $\varepsilon = 10^{-5}$, which is very small compared with the mean values of the flow. The nozzle flow is modelled by the 1D Euler equations with variable nozzle area

$$\frac{\partial \mathbf{U}}{\partial t} + \frac{\partial \mathbf{F}(\mathbf{U})}{\partial x} = -\frac{1}{A}\frac{\mathrm{d}A}{\mathrm{d}x}\mathbf{U}' \tag{77}$$

$$\mathrm{U} \equiv [\rho, \rho u, e]^{\mathrm{t}}, \quad \mathrm{F} \equiv [\rho u, \rho u^2 + p, \rho u H]^{\mathrm{t}}, \quad \mathrm{U}' \equiv [\rho u, \rho u^2, \rho u H]^{\mathrm{t}}$$

DOI: 10.1002/fld

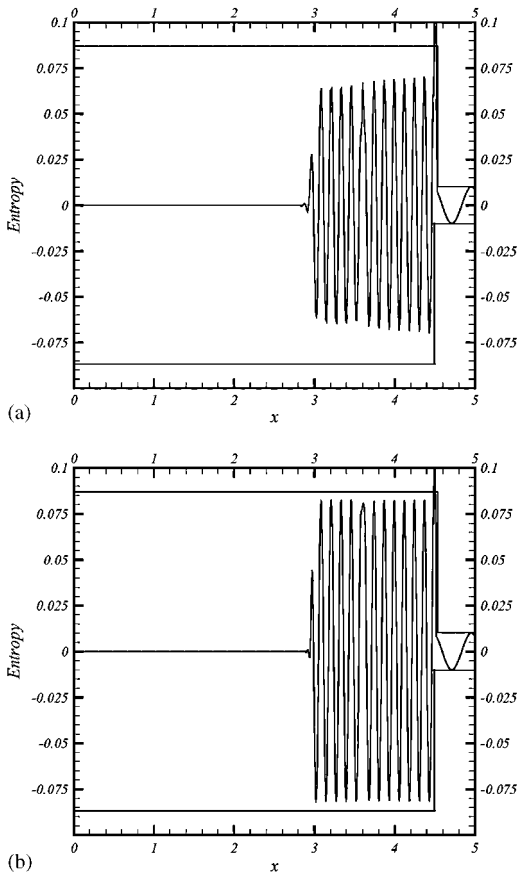

Figure 18. Shock/entropy wave interaction: $t=1.12687$, $k=13$, CFL$=0.25$ Hermite-HLLC scheme: (a) $N=400$ and (b) $N=800$.

The area of the nozzle, $A(x)$, is defined to be

$$A(x)=\begin{cases}0.536572-0.198086\times\exp\left(-\mathrm{Log}(2)\left(\dfrac{x}{0.6}\right)^2\right), & x>0\\ 1.0-0.661514\times\exp\left(-\mathrm{Log}(2)\left(\dfrac{x}{0.6}\right)^2\right), & x<0\end{cases}$$

Flow variables are non-dimensionalized by using the upstream values. The velocity scale is a_∞ (speed of sound), the length scale is D (diameter of the nozzle) and the density scale is the static density, ρ_∞.

Then, the mean flow at the inlet is

$$\begin{bmatrix}\overline{\rho}\\ \overline{u}\\ \overline{p}\end{bmatrix}_{\text{inlet}}=\begin{bmatrix}1\\ M_\infty\\ 1/\gamma\end{bmatrix} \tag{78}$$

DOI: 10.1002/fld

The Mach number at the inlet, M_∞, is 0.2006533 and the pressure at the exit, p_{exit}, is 0.6071752, so that a shock is formed inside the nozzle. The shock location is then: $x_s = 0.3729$.

Just upstream of the shock wave, the Mach number is $M_1 = 1.465$ and downstream, $M_2 = 0.714$. The pressure ratio (intensity of the shock wave) is then $p_2/p_1 = 2.337$.

The incoming acoustic wave, with angular frequency, $\omega = 0.6\pi$, is described as

$$\begin{bmatrix} \rho \\ u \\ p \end{bmatrix}_{\text{acoustic}} = \varepsilon \begin{bmatrix} 1 \\ 1 \\ 1 \end{bmatrix} \sin\left[\omega\left(\frac{x}{1+M_\infty} - t\right)\right] \tag{79}$$

The acoustic perturbations for the first derivatives are deduced from (79).

In the present work, the acoustic wave will be computed directly by solving the nonlinear governing equations rather than solving the linearized equations (see [19] for some examples on the linearized problem). This makes it harder to compute the acoustic waves. The challenge is whether the small amplitude wave can still be captured into the computation by the Hermite-HLLC scheme. The computational domain is $-10 \leqslant x \leqslant 10$ and a non-uniform mesh, refined in the throat region, is used.

To begin with, the steady state of the nozzle flow is computed. For the flow variables, the initial conditions are specified by using the mean exact solution of this problem.

The derivatives are then estimated by using a centred second-order finite-difference approximation. At the boundaries, the back pressure is specified at the outlet and the total pressure and density are specified at the inlet. The other needed information at both the inlet and outlet, are obtained using extrapolation from their neighbouring mesh points. Concerning the derivatives, all those quantities are set to zero at the inlet since the flow is assumed uniform. At the outlet, the pressure derivative is set to zero while the remaining quantities are extrapolated in order for the error to leave the computational domain without numerical reflections.

The steady-state solution of (77), obtained using a 180 points non-uniform mesh ($\Delta x_{\min} = 6.74 \times 10^{-2}, \Delta x_{\max} = 0.35$) with CFL = 0.80, is compared with the exact solution, Figure 19(a). The solution is converged to machine precision, Figure 19(b). It can be seen that flow properties are uniform in most regions of the nozzle, but change dramatically near the nozzle throat, Figure 19(a). Lastly, the shock is captured without any numerical oscillation.

After the steady-state flow-field is computed, the acoustic wave propagation can be simulated using the same nonlinear solver.

First, the initial conditions are specified using the steady-state solution previously calculated, then, at the inlet, the solution (79) is superimposed for the variables and its derivatives.

Numerical solutions of the acoustic pressure at $t = 14T$ are shown in Figure 19(c) and compared with the analytical solution (given in [19]).

With $N = 180$ grid points, the wave pattern is correctly captured by the Hermite-HLLC scheme, Figure 19(c). However, the amplitude of the acoustic wave at the shock location is larger than that indicated by the analytical solution: this is due to a slight oscillation introduced by the scheme just at this place.

To improve these results, one can try to optimize the value of α for this particular test. Figure 20 displays new numerical results obtained with $\alpha = 10$. As one can see, results are improved at the location of the discontinuity, Figure 20(a), although a slight amplification is still present. In spite of this difficulty, one can note that the profiles of the acoustic pressure both upstream

DOI: 10.1002/fld

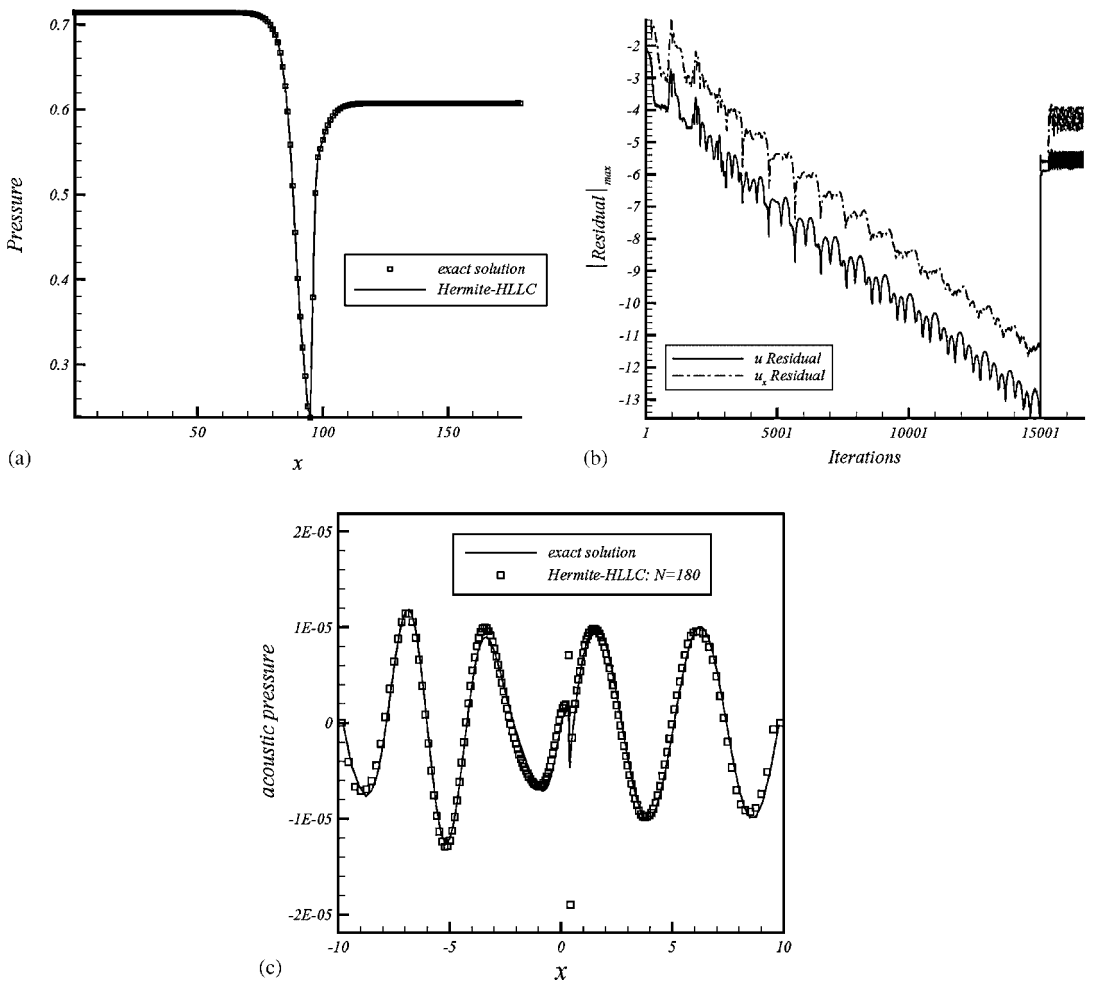

Figure 19. Propagation of sound waves through a transonic nozzle. HLSM-Minmod scheme: CFL = 0.8, $N = 180$, $\alpha = 2$, $\Delta x_{\min}/\Delta x_{\max} = 0.192$: (a) steady-state solution: mean pressure; (b) maximum residual; and (c) acoustic pressure at $t = 14T$.

and downstream the shock location, agree very well with the analytical solution, Figures 19(c) and 20(a).

As it is known, any high-order scheme captures the shock with a first-order accuracy [20]; however, these results demonstrate that this drawback does not alter the smooth part of the solution: the multi-scale structure of the solution is preserved after having crossed the shock wave. In other words, this result means that the numerical error generated by capturing the shock remains confined and does not propagate. Thus, this property explains the good results obtained with the HLSM reconstruction. The main advantage of such an interpolation comes from its compactness and the definition of its nonlinear weight, w_i, defined to modulate the monotonicity constraints: this enables to generate a local first-order correction when a discontinuity appears.

DOI: 10.1002/fld

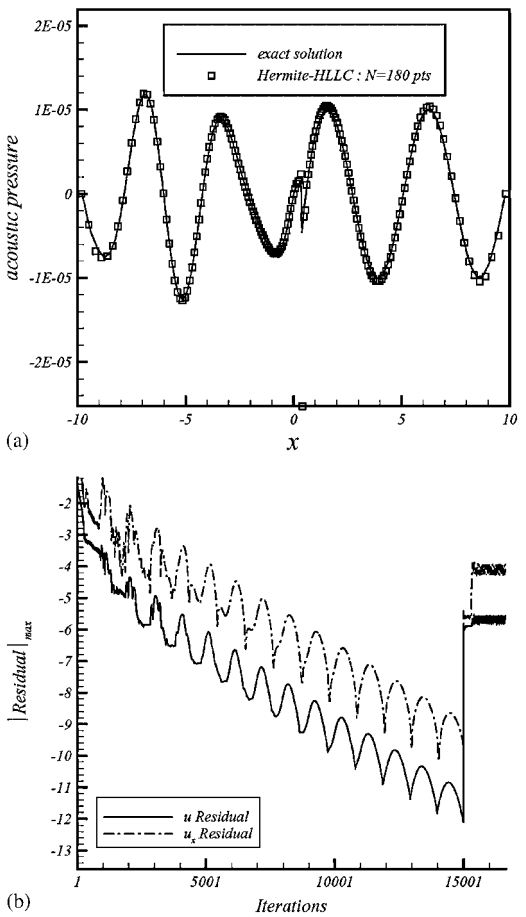

Figure 20. Propagation of sound waves through a transonic nozzle. Acoustic pressure at $t = 14T$ HLSM-Minmod scheme. $\alpha = 10$: (a) acoustic pressure and (b) maximum residual.

6. CONCLUDING REMARKS AND PERSPECTIVES

The purpose of this article was to develop a numerical method that enables to compute with accuracy, complex flows with, possibly, embedded discontinuities, on irregular meshes.

To this aim, we decomposed this problem in two parts.

In the first part, we constructed a Hermite least-square monotone (HLSM) interpolation for 1D hyperbolic conservation laws. This new technique is aimed to deal with irregular meshes while preserving high-order accuracy.

When the solution is smooth, this procedure generates a fifth-order spatial accuracy. In regions of discontinuities, two additional numerical constraints are introduced in the Hermite least-square system. These constraints impose that the high-order reconstruction locally coincides with a low-order monotone reconstruction. To emulate these monotonicity constraints only in regions of non-smooth data, we developed a data-depending weight. According to the magnitude of this weight,

DOI: 10.1002/fld

the monotonicity constraints are either discarded (the resulting scheme is fifth-order accurate) or emphasized (the scheme locally behaves as a first-order scheme).

In addition, we introduced into the definition of this weight, a parameter that we called the 'monotonicity parameter'. This parameter is devised to control the numerical dissipation at the location of a discontinuity. Accuracy and spectral analysis combined with numerical investigations gave us the following significant results:

- In regions of discontinuities, the spatial truncature error becomes first order, resulting in a monotone behaviour of the scheme. Increasing the monotonicity parameter results in an increase of the numerical dissipation of the scheme. However, this dissipative term is bounded by that of an upwind first-order scheme.
- When the solution is smooth, the monotonicity parameter has no influence on the accuracy of the scheme.
- The way of initializing the first derivative has no influence neither on the accuracy of the scheme nor on its stability.
- On irregular meshes, the scheme efficiently calculates multi-scale problems without generating too much numerical dissipation.
- Because of an increased algebraic complexity, the numerical method is costly when compared with schemes that are more classical.

In the second part, we developed the 'Hermite-HLLC' scheme that introduces a third wave in the classical HLL Riemann solver and that is devised to utilize the HLSM interpolation procedure. The third wave we introduced enables to discriminate between a shock wave and a contact wave; in addition, this contact wave is defined so that the first derivatives also verify Rankine–Hugoniot conditions. Numerical experiments about isolated discontinuities gave promising results. Finally, numerical results obtained for flow with complex patterns, showed the versatility of the numerical method.

However, the CPU time effort of the resulting method remains significant. This is mainly because the monotonicity constraints, introduced within the least-square system, necessitate inverting this system at each run time. Least-square methods that are more classical use pre-computed geometric coefficients within the reconstruction.

This point should be improved in the future. A possible solution would be to define an adaptive procedure that, according to the magnitude of the monotonicity sensor, would use the geometric coefficients of the pre-inverted least-square system, when the solution is smooth, and would invert the modified least-square system only in regions of discontinuities. Unfortunately, preliminary numerical results using this strategy showed the existence of numerical instabilities in regions close to the discontinuity: clearly, the monotonicity sensor used in this article, should be redefined in order to generate a smoother transition between the continuous part of the solution and its discontinuous part.

However, in spite of its limits and insufficiencies, the method we promoted has the advantage to be adaptive. First, the method is adaptive because numerical constraints can be added or modified easily, to control the monotonicity of the scheme; then, because the use of a least-square formulation enables to deal with irregular meshes. Lastly, because the Hermite-HLL procedure can be adapted, either by modifying the calculation of the characteristic wave speeds or by changing the physical definition of the contact discontinuity.

In our next future work, we shall try to extend some features of this method to multi-dimensional hyperbolic problems. To reach this target, the final step will be to formulate truly

DOI: 10.1002/fld

multi-dimensional monotonicity constraints, since TVD principles we used in this paper are intrinsically 1D constraints. Those monotonicity constraints will be devised in order to reduce the computational effort of the resulting method, for example by using the strategy already mentioned above.

However, before doing that, we shall develop, an intrinsically multi-dimensional Riemann solver, for example by adapting to a Hermite problem, ideas such as those developed in the 'fluctuation-splitting approach' [21]. In that case, the benefit hoped will be an improvement of the handling of discontinuities or strong expansions when those waves lie oblique to the grid.

APPENDIX A: SPECTRAL ANALYSIS FOR THE HERMITE SCHEME

This study required the intensive use of the MAPLE symbolic mathematical computer package.

We start this analysis from the linear semi-discrete form (69):

$$\left.\frac{\mathrm{d}U}{\mathrm{d}t}\right|_i + a \times \frac{U^{\mathrm{l}}_{i+1/2} - U^{\mathrm{l}}_{i-1/2}}{\Delta x} = 0 \tag{A1}$$

This form is supposed to be the discretized form, by the HLSM method, of Equation (68). Now, assuming that the calculation domain is periodic, we decompose the discrete vector solution, $U_i \equiv (\overline{u}_i, \overline{r}_i)^{\mathrm{t}}$, in Fourier series

$$U_i = \hat{U} \times \mathrm{e}^{\mathrm{j}kx_i} \quad (j^2 = -1) \tag{A2}$$

Where $\hat{U} \equiv (\hat{u}, \hat{r})^{\mathrm{t}}$ represents the complex amplitude of the vector solution and k, the wave number of the periodic signal.

Inserting (A2) into (A1) produces the following result:

$$\frac{\mathrm{d}\hat{U}}{\mathrm{d}t} = G(\beta, v, \alpha) \times \hat{U} \tag{A3}$$

$G(\beta, v, \alpha)$ is a complex 2×2 matrix that represents the discrete Fourier transform of the spatial operator in (A1). This matrix only depends upon the phase angle, β ($\equiv k\Delta x$), the CFL number, v ($\equiv a\Delta t/\Delta x$) and the 'monotonicity parameter', α.

To explicitly formulate $G(\beta, v, \alpha)$, we need to develop the characteristics of the HLSM scheme.

Thus, the HLSM reconstruction necessitates inverting the following 6×4 linear least-square problem:

$$L \times X = B \tag{A4}$$

with

$$L \equiv [L_{ij}]^{\mathrm{t}}_{j \in \{1,\ldots,6\}}\text{: metric terms (modified by } w_i \text{ for } L_{i5,6})$$

$$X \equiv [\{\tilde{a}_j\}_{j \in \{1,2,3,4\}}]^{\mathrm{t}}\text{: polynomial coefficients}$$

$$B \equiv [\overline{u}_{i-1} - \overline{u}_i, \overline{u}_{i+1} - \overline{u}, \overline{r}_{i-1} - \overline{r}_i, \overline{r}_{i+1} - \overline{r}, w_i \times B_5, -w_i \times B_5]^{\mathrm{t}}\text{: numerical constraints}$$

DOI: 10.1002/fld

To get an analytical solution for X, system (A4) is partially inverted via a Gram–Schmidt process. In this manner, system (A4) becomes

$$R \times X = Q^{\mathrm{t}} \times B \tag{A5}$$

Where Q is a symmetric and orthogonal 6×6 matrix resulting from the $L = Q \times R$ decomposition; R is an upper-triangular 4×6 matrix. Both matrices only depend upon the metric terms identified by Equations (15). The monotonicity parameter, α, explicitly appears in those terms through the introduction of the weight, w_i.

Therefore, inserting (A2) into (A5), the resulting system can be explicitly solved for the vector $\hat{X} \equiv [\{\hat{a}_j\}_{j\in\{1,2,3,4\}}]^{\mathrm{t}}$, which now represents the Fourier transform of the initial vector, $X(\{\hat{a}_j\} \equiv$ Fourier transform of the space derivatives, $\{\tilde{a}_j\})$.

Thus, we get in the Fourier space the following result:

$$\hat{X} = \mathscr{L}(\beta, \alpha) \times \hat{U} \quad (\beta \equiv k \times \Delta x) \tag{A6}$$

Then, by using this result, it becomes possible to evaluate the Fourier transform of the interpolated values $(\hat{u}^{\mathrm{I}}_{i+1/2}, \hat{r}^{\mathrm{I}}_{i+1/2})$:

$$\begin{aligned} \hat{u}^{\mathrm{I}}_{i+1/2} &= \left(\hat{u} + \hat{a}_1 \frac{\Delta x}{2} + \hat{a}_2 \frac{\Delta x^2}{6} + \hat{a}_3 \frac{\Delta x^3}{8} + \hat{a}_4 \frac{\Delta x^4}{20}\right) \times \mathrm{e}^{\mathrm{j}kx_i} \\ \hat{r}^{\mathrm{I}}_{i+1/2} &= \left(\hat{r} + \hat{a}_2 \Delta x + \hat{a}_3 \frac{\Delta x^2}{2} + \hat{a}_4 \frac{\Delta x^3}{2}\right) \times \mathrm{e}^{\mathrm{j}kx_i} \end{aligned} \tag{A7}$$

Consequently, evaluating the expression: $a\Delta t \times (\hat{U}^{\mathrm{I}}_{i+1/2} - \hat{U}^{\mathrm{I}}_{i-1/2})/\Delta x$, one can explicitly formulate the complex matrix, $G(\beta, v, \alpha)$, in (A3); this matrix is too complicated to be formulated in this article. Finally, integrating (A3) by the third-order TVD Runge–Kutta scheme, (10), over the interval $[t_n, t_{n+1}]$, produces the following result:

$$\hat{U}^{n+1} = \mathscr{G}(\beta, v, \alpha) \times \hat{U}^n \tag{A8}$$

where

$$\mathscr{G}(\beta, v, \alpha) \equiv [\mathrm{Id} + G \times [\mathrm{Id} + \tfrac{1}{2} G \times [\mathrm{Id} + \tfrac{1}{3} G]]]$$

is a 2×2 complex matrix; Id represents the 2×2 identity matrix.

$\mathscr{G}(\beta, v, \alpha)$ is called the 'amplification matrix' of the scheme and makes it possible to analyse the numerical properties of the HLSM discretization.

For this purpose, the exact amplification matrix for (68) must be specified. Using a continuous Fourier transform of (68), we get the differential form

$$\frac{\mathrm{d}\hat{U}}{\mathrm{d}t} + \mathrm{j}ka \times \hat{U}(t) = 0 \tag{A9}$$

Integrating, exactly, this form between t_n and t_{n+1}, we obtain

$$\hat{U}^{n+1} = \mathrm{e}^{-\mathrm{j}v\beta} \times \hat{U}^n \tag{A10}$$

DOI: 10.1002/fld

Specifically, if $U(x, t=0)=[\cos kx, -k\sin kx]^{\mathrm{t}}$, then the relation that follows can be obtained from (A10):

$$\hat{U}^{n+1}=\begin{bmatrix}1\\ \dfrac{j\beta}{\Delta x}\end{bmatrix}\times \mathrm{e}^{-\mathrm{j}(n+1)\nu\beta} \tag{A11}$$

From this result, we can identify the following quantities:

$$\begin{aligned} r_{\mathrm{e}}(\beta) &\equiv [1, j\beta/\Delta x]^{\mathrm{t}}\\ \lambda_{\mathrm{e}}(\beta,\nu) &\equiv \mathrm{e}^{-\mathrm{j}\nu\beta}\\ \hat{w}_{\mathrm{e}}(\beta,\nu) &\equiv 1 \end{aligned} \tag{A12}$$

$\lambda_{\mathrm{e}}(\beta,\nu)$ represents the exact eigenvalue of system (68), $r_{\mathrm{e}}(\beta)$ is its associated eigenvector while $\hat{w}_{\mathrm{e}}(\beta,\nu)$ represents the complex amplitude of the exact solution.

Now, returning to the amplification matrix, $\mathscr{G}(\beta,\nu,\alpha)$, we can calculate its eigenvalues: $\lambda_1(\beta,\nu,\alpha)$ and $\lambda_2(\beta,\nu,\alpha)$.

Defining $\Lambda\equiv\mathrm{diag}[\lambda_1,\lambda_2]$, one can also write: $\mathscr{G}\equiv\mathscr{R}\Lambda\mathscr{R}^{-1}$; where the matrix $\mathscr{R}$ is defined as the matrix of the right eigenvectors of $\mathscr{G}(\beta,\nu,\alpha)$: $\mathscr{R}\equiv[r_1(\beta,\nu), r_2(\beta,\nu)]^{\mathrm{t}}$.

Finally, by defining $\hat{W}\equiv[\hat{w}_1,\hat{w}_2]^{\mathrm{t}}\equiv\mathscr{R}^{-1}\times\hat{U}$ and inserting this definition into relation (A8), one obtains by recurrence

$$\hat{U}^{n+1}=\lambda_1^{n+1}\hat{w}_1^0\hat{r}_1+\lambda_2^{n+1}\hat{w}_2^0\hat{r}_2 \tag{A13}$$

By definition, the first component of the right-hand term is called the 'accurate component' of the numerical solution. In other words, if we compare (A11) with (A13), the quantity $\lambda_1^{n+1}\hat{w}_1^0\hat{r}_1$ represents the approximation of the quantity $[1, j\beta/\Delta x]^{\mathrm{t}}\times\mathrm{e}^{-\mathrm{j}(n+1)\nu\beta}$. More precisely, using (A12) we can specify the following approximations:

$$\begin{aligned} \lambda_1(\beta,\nu,\alpha) &\sim \mathrm{e}^{-\mathrm{j}\nu\beta}\\ r_1(\beta,\nu,\alpha) &\sim [1, j\beta/\Delta x]^{\mathrm{t}}\\ \hat{w}_1(\beta,\nu,\alpha) &\sim 1 \end{aligned} \tag{A14}$$

Practically, the 'accurate eigenvalue', $\lambda_1(\beta,\nu,\alpha)$, is identified from $\mathscr{G}(\beta,\nu,\alpha)$ by using the consistency condition

$$\lambda_1(\beta,\nu,\alpha)\underset{\beta\to 0}{\to}1 \tag{A15}$$

Then, its associated eigenvector, $r_1(\beta,\nu,\alpha)$, can be evaluated. $\hat{w}_1^0$, which represents the complex amplitude at $t=0$, of the accurate component of the solution, is calculated from the initial conditions for $\hat{U}^0$.

For example, if $U(x, t=0)\equiv[\cos kx, -k\sin kx]^{\mathrm{t}}$ and if this initial condition is approximated by a second-order centred discretization, then we obtain the result

$$\hat{U}^0=[1, j\sin\beta/\Delta x]^{\mathrm{t}} \tag{A16}$$

DOI: 10.1002/fld

Therefore, by writing (A13) at $t=0$, we obtain the relation

$$\hat{U}^0 = \hat{w}_1^0 r_1 + \hat{w}_2^0 r_2 \tag{A17}$$

By using (A16), system (A17) is easily inverted to determine $\hat{w}_{1,2}^0$.

By contrast, the remaining component on the right-hand side of (A13) is called the 'spurious component' of the numerical solution. This component is a general characteristic of extended algebraic systems that use auxiliary variables—in our case, the first derivative of the solution—and has no counterpart in the differential problem. This component represents the behaviour of the numerical error introduced either at the boundaries or at $t=0$, by the approximation of the first derivative; it can also be excited on highly distorted meshes.

The spurious component of the numerical solution must be damped in time, whatever the mesh, so that the accurate part of the solution is not affected. For a more detailed explanation about the notion of 'spurious component' and its behaviour, we refer the interested reader to [1].

Finally, knowing the analytical form of $\mathcal{G}(\beta, v, \alpha)$, the spectral analysis of the HLSM scheme can be fully managed by defining the following quantities:

- the discretization error at $t=t_n$: $|e^{-jnv\beta} - \lambda_1^n \hat{w}_1^0 r_1|$,
- the spurious error at $t=t_n$: $|\lambda_2^n \hat{w}_2^0 r_2|$,
- the truncature error (space and time): $|e^{-jv\beta} - \lambda_1|/\beta$,
- the amplitude error: $1-|\lambda_1|$,
- the phase error: $|1+\mathrm{Arg}(\lambda_1)/v\beta|$.

These quantities are parameterized by the number of cells-per-wavelength, N ($N\times\beta=2\pi$), the CFL number, v and the monotonicity parameter, α.

ACKNOWLEDGEMENTS

The author wishes to thank with recognition, Dr G. B. Deng (Ecole Centrale de Nantes—France) who provided all technical support essential to this work.

REFERENCES

1. Van-Leer B. Towards the ultimate conservative difference scheme IV. A new approach to numerical convection. *Journal of Computational Physics* 1977; **23**:276–299.
2. Harten A, Engquist B, Osher S, Chakravarthy S. Uniformly high order accurate essentially non-oscillatory schemes, III. *Journal of Computational Physics* 1987; **71**(2):231–303.
3. Liu X-D, Osher S, Chan T. Weighted essentially non-oscillatory schemes. *Journal of Computational Physics* 1994; **115**:200–212.
4. Shu C-W. Essentially non-oscillatory and weighted essentially non-oscillatory schemes for hyperbolic conservation laws. *ICASE Report 97-65*, 1997.
5. Barth TJ. *Aspects of Unstructured Grids and Finite-volume Solvers for the Euler and Navier–Stokes Equations*, VKI Lecture Series, 1994.
6. Barth TJ. Recent developments in high-order *k*-exact reconstruction on unstructured meshes. *AIAA Paper 93-0668*, January 1993.
7. Ollivier-Gooch CF. Quasi-ENO schemes for unstructured meshes based on unlimited data-dependent least-squares reconstruction. *Journal of Computational Physics* 1997; **133**:6–17.
8. Capdeville G. A Hermite upwind WENO scheme for solving hyperbolic conservation laws. *Journal of Computational Physics* 2008; **227**:2430–2454.

DOI: 10.1002/fld

9. Einfeldt B, Munz CD, Roe PL, Sjögreen B. On Godunov-type methods near low densities. *Journal of Computational Physics* 1991; **92**:273–295.
10. Toro EF, Spruce M, Spears W. Restoration of the contact surface in the HLL Riemann solver. *Shock Waves* 1994; **4**:25–34.
11. Shelkovich VM. The Riemann problem admitting δ-, δ'-shocks and vacuum states (the vanishing viscosity approach). *Journal of Differential Equations* 2006; **231**:459–500.
12. Shu C-W, Osher S. Efficient implementation of essentially non-oscillatory shock-capturing schemes. *Journal of Computational Physics* 1988; **77**:439–471.
13. Toro EF. *Riemann Solvers and Numerical Methods for Fluid Dynamics*. Springer: Berlin, 1997.
14. Batten P, Clarke N, Lambert C, Causon DM. On the choice of wavespeeds for the HLLC Riemann solver. *SIAM Journal on Scientific Computing* 1997; **18**:1553–1570.
15. Qiu J, Shu C-W. Hermite WENO schemes and their applications as limiters for Runge–Kutta discontinuous Galerkin method: one-dimensional case. *Journal of Computational Physics* 2004; **193**:115–135.
16. Qiu J, Shu C-W. On the construction, comparison, and local characteristic decomposition for high-order central WENO schemes. *Journal of Computational Physics* 2002; **183**:187–209.
17. Mc Kenzie J, Westphal K. Interaction of linear waves with oblique shock waves. *Physics of Fluids* 1968; **11**:2350–2362.
18. Zang TA, Hussaini MY, Bushnell DM. Numerical computations of turbulence amplification in shock wave interactions. *AIAA Journal* 1984; **22**:13–21.
19. Third computational aeroacoustics workshop on benchmark problems. NASA/CP-2000-209790.
20. Hindman RG. On shock-capturing methods and why they work. *AIAA-Paper-88-0622*, 1988.
21. Paillère H. Multidimensional upwind residual distribution schemes for the Euler and Navier–Stokes equations on unstructured grids. *Ph.D. Thesis*, Université Libre de Bruxelles, 1995.

DOI: 10.1002/fld